Hydrodynamic Analysis and Classification of Large Dense Planar Synchronous Fish Schools

_____

A Thesis

Presented to

the faculty of the School of Engineering and Applied Science

University of Virginia

_____

In Partial Fulfillment

of the requirements for the Degree

Master of Science in Mechanical and Aerospace Engineering

By

John Kelly

November 2022

APPROVAL SHEET

The thesis is submitted in partial fulfillment of the
requirements for the degree of
Master of Science

_____
John Kelly, Author

This thesis has been read and approved by the examining Committee:

_____
Haibo Dong, Advisor

_____
Daniel Quinn, Committee Chair

_____
Qing Chang, Committee Member

_____
Joseph Zhu, Committee Member

Accepted for the School of Engineering and Applied Science:

_____
Jennifer L. West, Dean
School of Engineering and Applied Science

December 2022

Abstract

As our understanding of fish schooling as a mechanism for increased speed and efficiency deepens, the need arises for hydrodynamic analysis of fish schools to grow beyond the smaller models using a few fish commonly seen in literature towards the larger schools observed in nature. To that end, the fluid interactions in a large dense planar synchronous fish school ($n \geq 10$) are studied in this work. Numerical simulations of two-dimensional carangiform swimmers are used to observe the hydrodynamics of large fish schools. It is shown that the average efficiency of the 10-fish school swimming is increased by 30% over a solo swimmer, along with a thrust production improvement of 114%. The performance of each fish is analyzed in depth, and several primary interaction mechanisms are uncovered. Anterior body suction arises from the proximity of the suction side of the flapping tail to the head of the next fish, which occurs throughout the school. The block effect persists in the back of the school and an enhanced block effect is shown as subsequent fish are added behind. The partial block effect is also demonstrated along the edges of the school. The wall effect is proven to enhance the flow of momentum downstream and thus increase the net forward force of the school. This occurs throughout the school and is further enhanced by a vortex pair aiding the lateral advection beyond the subsequent fish bodies at the edge of the

school. Because these primary body-body interactions are based on the arrangement of surrounding fish, a classification of individual fish within the school arises based on the interactions for each group and is reflected in the performance of the individuals. It is shown that the school can be separated into the front fish, middle fish, edge fish, and back fish. These groupings and mechanisms observed are proven to be consistent over a range of Reynolds numbers and school sizes. Finally, the effects of increasing the length of the school by adding fish in the streamwise direction are tested. It is shown that efficiency and net thrust continue to increase when adding fish; however, the net thrust starts to decrease above 16 fish in the school and a limit of efficiency is approached. This is shown to occur due to vortex structure breakdown and loss of the anterior body suction on the edge of the school.

This thesis is dedicated to my parents and grandparents,

for their endless love and support of my goals.

Acknowledgements

First, I would like to say thank you to Dr. Haibo Dong, whose guidance and expertise were essential to my technical development and the work in this thesis. I would also like to thank Alec Menzer, Jiacheng Guo, Yuchen Gong, Yu Pan, Dr. Junshi Wang, Dr. Pan Han, Dr. Wei Zhang, and all former members of FSRG for their advice, technical advancements, and examples set by their own research that made this work possible. A special thank you to Yu, who worked with me closely on much of the work presented here, and whose feedback and advice have been essential to this thesis and my growth as a researcher. I would also like to thank my committee members, along with the other faculty in the Mechanical and Aerospace department for their support. Dr. Matthew Barry, my undergraduate research advisor from University of Virginia, also deserves a thanks for introducing me to the world of research and inspiring me to pursue it further. Finally, thank you to my family for their constant love and support.

Contents

List of Figures

List of Tables

1 Introduction

Fish schooling is motivated by a variety of factors, including predator defense, reproduction, socialization, and hydrodynamic benefits [1]. As engineers, we are most interested in the hydrodynamics of fish schooling for its application in our underwater vehicles. Significant progress has been made in optimizing these vehicles for both speed and efficiency [2], but more advancements are required in understanding fish schooling to fully optimize larger groups of them. Additionally, there is a fundamental interest from biologists in better understanding the hydrodynamics of fish schooling. Finally, discoveries from studying large fish schools can be utilized in other fluids applications containing a large number of interacting bodies.

1.1 2 Fish Interaction Hydrodynamics

To understand fish schooling from a hydrodynamics perspective, many studies have utilized 2 fish systems. They employ two-dimensional (2D) and three-dimensional (3D) computational simulations and experiments to investigate fluid dynamics, stability, and control in a simplified 2 fish system. To begin, the hydrodynamics and wake classification of 2 fish swimming side-by-side were completed by Dong et al. [3].

They found that in-phase swimming provided power saving for the system, while anti-phase swimming led to an enhancement in the forward forces generated. Khalid et al. studied the effect of Strouhal number and phase speed on two fish swimming in-line [4]. It was found that swimming in tandem led to an enhancement in performance for the upstream fish due to wake splitting by the rear fish increasing the pressure behind the upstream fish. A drafting effect benefiting the trailing fish is also observed for some conditions. Stable 2D arrangements of flapping foils were studied by Lin et al. [5]. By varying flapping parameters and phase they discovered that stable arrangements can largely be split into semi-tandem and staggered arrangements, and the semi-tandem formations led to higher propulsive efficiencies and speed. Research from Novati et al. shows that for a simplified 2D system of 2 fish, reinforcement learning (RL) can be used to control the follower to optimize the efficiency of the follower [6]. This led to a 30% reduction in the energy used to move a set distance. Verma et al. similarly utilized RL on 2 and 3 fish systems, in both 2D and 3D [7]. They concluded that a control algorithm could be developed based on the RL results, and the efficiency of the motion is increased by the interaction of vortex from the upstream fish interacting with the midsection of the follower's body in both the 2D and 3D results. Li et al. studied 3D simulations of two fish swimming and varied the planar spatial arrangement, finding that stability and efficiency are heavily dependent on the arrangement and phase of the fish [8]. They identify zones of high cost-of-transport in the wake of the leader fish and suggest that some wake capturing can be beneficial to efficiency, while other wake intercepting is detrimental to the fish. Finally, hydrodynamics and wake structure in 3D arrangements of a 2-fish system was investigated by Pan et al. [9]. The study found
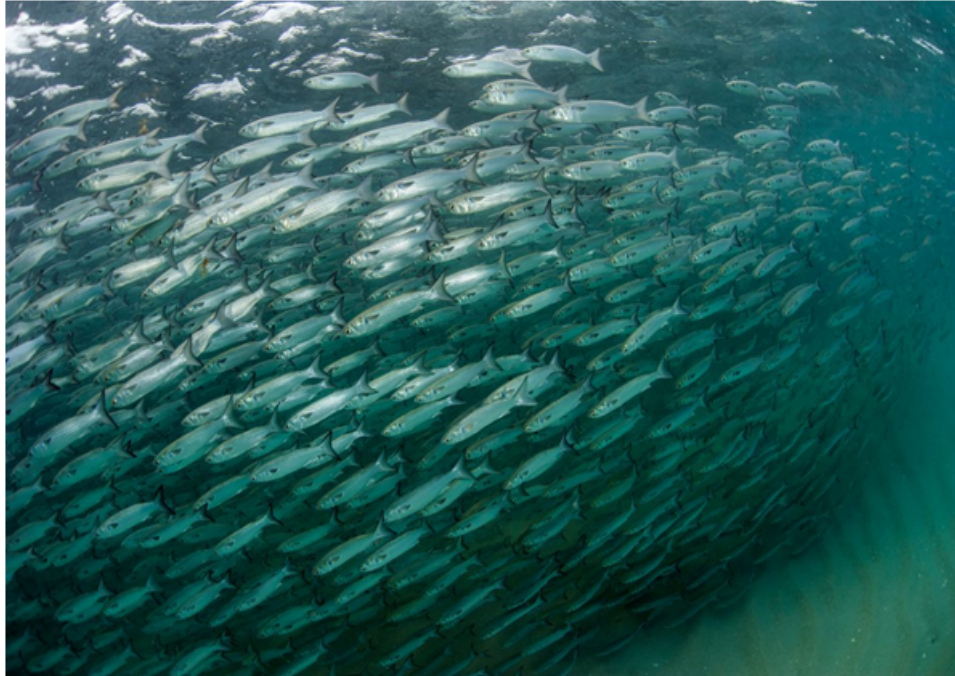
FIGURE 1.1: School of Mullet fish from Hakai Magazine [10].

that power consumption and drag on the trunk are disturbed by the flow interactions between fish. While all of these 2 fish systems give a solid background on fish-fish interactions using a simplified system, significant progress is still required to understand hydrodynamics within entire fish schools.

1.2 Fish School Studies

In real schools, the number of fish can reach millions like the example Mullet fish school shown in Fig. 1.1, and the arrangement of individual fish within the school varies significantly and fluctuates within a single school [11]. To study these larger schools, some progress in understanding has been made using lower-order models of
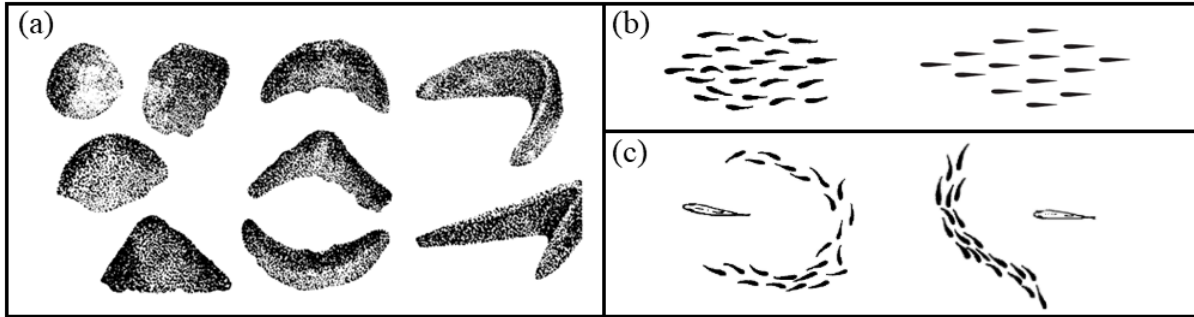
FIGURE 1.2: School arrangements from Kaganovsky [14](a) and Radakov [15](b-c), reproduced from Pavlov [11].

a large number of fish in a school. Gazzola et al. utilized a coupled reinforcement learning optimization of control of fish in large schools with a finite-width dipole method to model the interactions between swimmers [12]. Their work evaluated various arrangements of 100 swimmers, concluding that elongated school shapes allow for drafting and pushing to occur, improving the school's performance. Additionally, it was found that densely packed swimmers within the school gave the best opportunity to leverage interactions for performance benefit. Filella et al. published work that similarly uses a dipole method to approximate hydrodynamics for schools of 100 swimmers, finding that individuals in the school reached higher swimming speeds when including hydrodynamic interactions with the fish around it in the school [13]. While valuable for gaining initial information, the dipole method used in these studies cannot replace more accurate methods that robustly model the fluid interactions within these larger schools.

In addition to these lower-order methods, some work has been done in extending the previously mentioned 2 fish models into larger schools. Self propelled pitching foils, often used as an approximation for fish swimmers, have been observed as the number

of foils increases in different arrangements. A detailed analysis of thrust and efficiency enhancement due to in-line foil-foil interaction is given by Yuan et al [16] and Han et al. [17]. The former showed that this enhancement begins to reach a limit as the number of foils in-line gets to five. Saadt et al. furthered the work on in-line flapping foils by simulating an approximation for infinite foils, finding that hydrodynamic benefits of schooling in-line come from leading-edge suction on the trailing foil and added-mass push on the leading foil [18]. Finally, work was completed by Shelley et al., using a similar infinite school approximation to simulate infinite fish in-line as well as a phalanx, rectangular lattice, and diamond lattice formations, utilizing a model that captures essential features of the hydrodynamic interactions. They conclude that optimal benefit from hydrodynamic interactions comes from swimming in a lattice, with the streamwise spacing being the most important for performance benefit. Finally, there are a few works that detail hydrodynamics within larger school simulations. Dai et al. leverage numerical simulations of 2D fish with free swimming to investigate stable formations and energetics in schools with 2, 3, and 4 fish [19]. They found multiple stable arrangements for each, including an in-phase diamond arrangement. Their results suggest that passive stable arrangements of fish schools can be achieved via hydrodynamic interactions only, without leveraging any active control. Additionally, on the topic of diamond schools, Pan and Dong investigated spacing and phase in a diamond school arrangement [20], [21]. They found that the dense diamond school maximized interaction between fish, and attributed hydrodynamic benefits from schooling to a block effect, wall effect, body-body suction, and vortex capturing.

1.3   Project Overview

While significant progress has been made towards understanding hydrodynamics in schooling, it is clear that more work is needed utilizing a larger number of fish along with full fluids numerical simulations to uncover all of the mechanisms in effect for real fish schools. In this research, we utilize an immersed boundary method-based incompressible flow solver to simulate large (n $\geq$ 10) 2D fish schools in a variety of arrangements and Reynolds numbers. We demonstrate that distinct groups of individual fish performance emerge based on their location within the school. These are shown to be robust with changes in width, length, and Reynolds number. Additionally, the hydrodynamic basis for the arrangements is explored, giving the first high-fidelity analysis of fish-fish interaction within a large fish school. This work establishes a categorization that can be utilized for future research in the hydrodynamic analysis of large fish schools. Finally, the effect of increasing length by adding more fish to the school is explored, establishing a limit of efficiency increase by adding length to the dense school. The hydrodynamics behind the limit are investigated and the underlying mechanisms are uncovered.

1.4   Organization of Thesis

The structure of this thesis is as follows. The methodology for the fluids solver, validation for the solver, 2D fish swimming approximation, and performance parameters

are presented in Chapter 2. Chapter 3 details the results and mechanisms in a 10-fish school, presents the groupings of fish in the large school, and the mechanisms and groupings for varying Reynolds numbers and arrangements. Chapter 4 details the effect of length on school performance, investigating the limit of performance enhancement via longer schools and detailing the mechanisms that break down leading to a limit. Finally, Chapter 5 provides a summary of the work, its applications, and directions for future study.

2 Methodology

2.1 Numerical methods

In this study, the 2D unsteady viscous incompressible Navier-Stokes equations, written in index form as

$$\frac{\partial u_i}{\partial x_i} = 0; \quad \frac{\partial u_i}{\partial t} + \frac{\partial u_i u_j}{\partial x_j} = -\frac{\partial p}{\partial x_i} + \frac{1}{Re}\frac{\partial u_i^2}{\partial x_i \partial x_j}, \tag{2.1}$$

govern the flow. In the equations, p is pressure, u_i denotes Cartesian velocity components, and Re is the Reynolds number, given by the equation $Re = \frac{U_\infty c}{\nu}$. An in-house immersed boundary method-based finite difference flow solver is employed to solve the equations, which are discretized spatially using a cell-centered collocated arrangement of the primitive variables and integrated in time using a fractional step method, which is second-order accurate in time. The convection and diffusion terms are solved using an Adams-Bashforth scheme and implicit Crank-Nicolson scheme, respectively. The immersed boundary method utilizes a ghost-cell method to employ a complex interface boundary over a stationary Cartesian grid. A schematic is shown in Fig. 2.1. The process begins with identifying each cell on the cartesian grid. Fluid cells are cells

with the center outside the body, and solid cells are made of cells completely inside the body and not adjacent to the boundary. Ghost cells have a cell center inside the body and have neighboring cells outside the body. In order to preserve the boundary condition and maintain second order accuracy, a line is extended from the ghost cell through the boundary normal to the interface. An image point is defined as equidistant to the boundary intercept as the ghost cell center. An interpolation process is then used to calculate the values at the image point from the surrounding fluid cells, which is then used to obtain the value on the ghost cell. This method allows for simulation of complex moving boundaries on a stationary grid, without the computationally expensive re-meshing required by commercially available CFD solvers. It has been successfully employed in previous biological swimming studies [22]–[25] and bio-inspired canonical problems [17], [26]–[28], and has been previously validated extensively [17], [24], [29]. More details can be found in [30], [31].
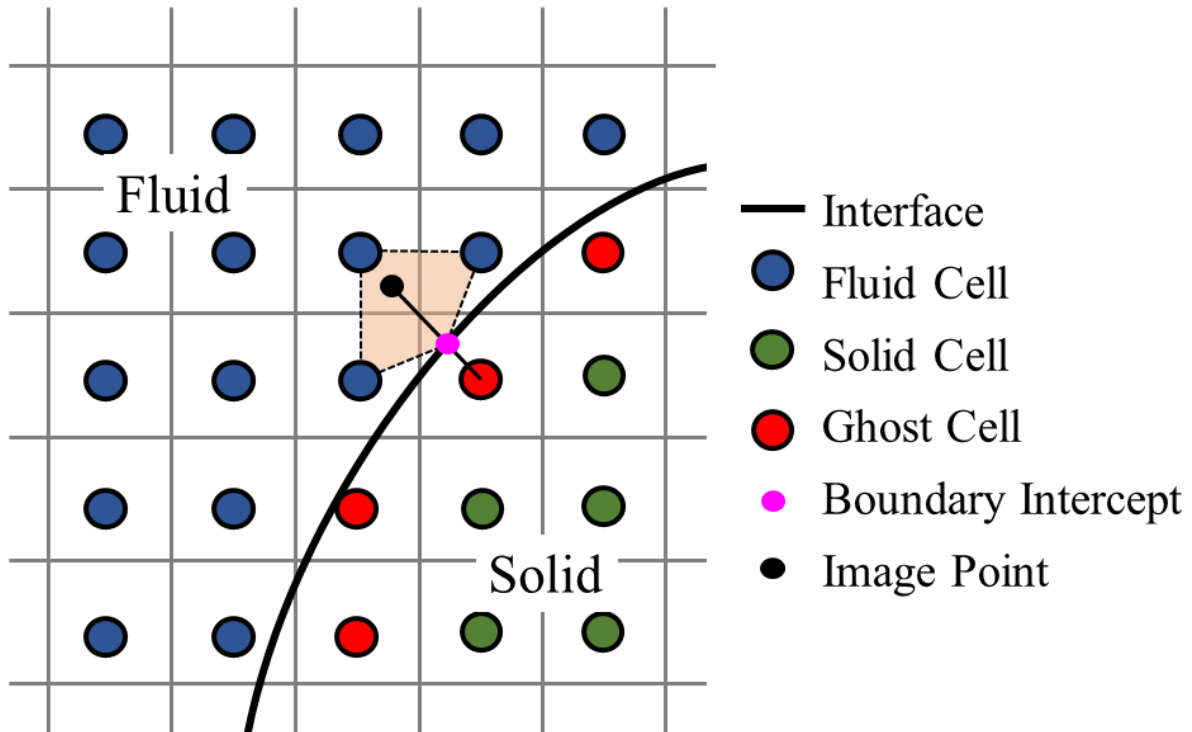
FIGURE 2.1: Schematic of Ghost Cell Immersed Boundary Method.

2.2 Validation

To further validate the computational solver for body-body interacting flows, the experimental work of Dewey et al. [32] is reproduced using the solver to verify its accuracy. In this experiment, Dewey studies two flapping foils in a side-by-side configuration, varying their phase and spacing at the Strouhal number of maximum efficiency (0.25). The foils span the entire depth of the water channel, mitigating their 3D effects and allowing a 2D computational approximation to compare closely with their results. A frictionless air bearing system is used alongside a load cell to measure the net thrust, used to calculate the thrust coefficient given in the results. PIV is also used to produce a vortex field and cycle-average velocity.
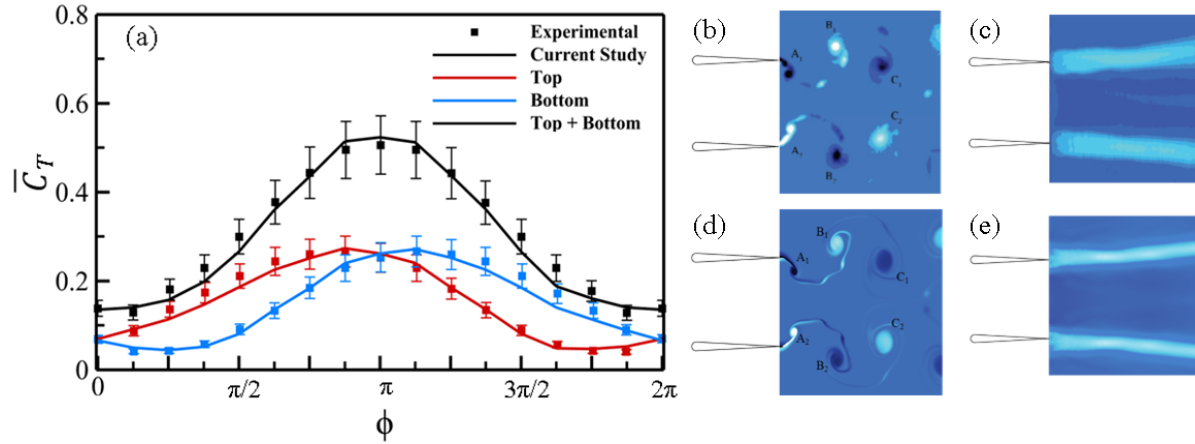
FIGURE 2.2: (a) Thrust coefficient of experimental results with error bars, along with the current computational study. Vorticity (b,d) and average velocity (c,e) from experimental results (top) and the computational results (bottom) for $\phi = \pi$.

The results from the experimental data along with the computational comparison from our solver are shown in Fig. 2.2. In part (a), the thrust coefficient for experimental data is given by the points, with the experimental error shown by the error bars, along with the computational data shown by the lines. From this, we see that almost every data point is within the experimental error. All points outside of the experimental error occur at very low values of C_T, where the experimental error range, which is given as a percentage by Dewey et al., is very small. This confirms the validity of our solver in calculating the hydrodynamic performance in multi-foil interacting systems. Parts (b) and (c) contain the vorticity and time-averaged velocity from the experimental data, and parts (d) and (e) are the same plots for the computational data. From the figure, both the vortex structure and the jets of the experimental and computational data match very closely, further validating our computational solver for wake analysis in multi-body interacting flows.

2.3 Fish-like kinematics

To define the fish-like motion for the study, a NACA0012 foil shape is used for the equilibrium state of the fish body. Traveling wave kinematics are then imposed on the foil, giving a resulting undulatory motion that mimics a top-down view of typical carangiform swimming. The body length is scaled to $l = 1$, and the lateral displacement is given by the equation:

$$y(x,t) = A(x) * sin(\frac{2\pi}{\lambda}x - \frac{2\pi}{T}t), \tag{2.2}$$

where the position variables, x and y, are normalized by the body length such that at the equilibrium state the midline of the fish body is a flat line at $y = 0$ spanning from $x = 0$ to $x = 1$. $y(x,t)$ represents the lateral deviation from this midline position during the undulating motion. T is the wave period of the traveling wave, and λ is the wavelength. $A(x)$ denotes the amplitude of the lateral wave, and is expressed by the following quadratic polynomial:

$$A(x) = a_2x^2 + a_1x + a_0, \tag{2.3}$$

where the coefficients are determined to be $a_0 = 0.02$, $a_1 = -0.08$, and $a_2 = 0.16$. These were determined by previous experimental data [33], and have been used in previous 2D computational studies of fish swimming [20], [34]. The wave amplitude envelope and resulting midline sequence through a cycle of motion are given in Fig. 2.3(a).
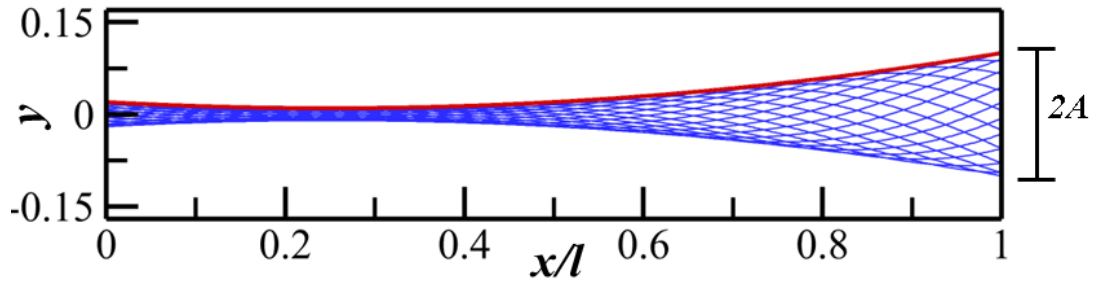
FIGURE 2.3: The traveling wave amplitude of a carangiform motion (red line) and the motions of the fish body mid-line during one tail-beat period (blue lines). A denotes the amplitude at the tail tip.
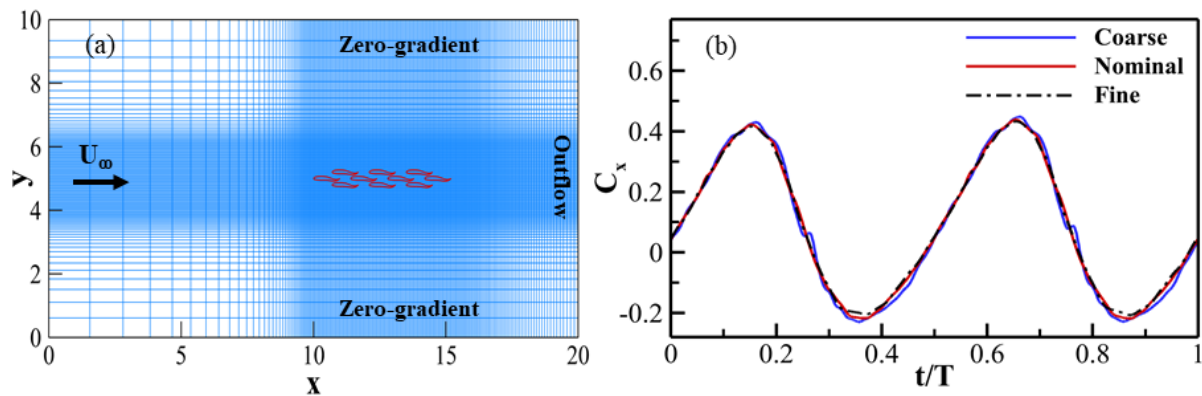
FIGURE 2.4: (a) Schematics of the computational domain, Cartesian grid, and boundary conditions. (b) Comparison of the instantaneous net-force coefficient of the last fish in the 10-fish school between the coarse, medium, and fine mesh.

2.4 Case Setup

A representative Cartesian grid is shown in Fig. 2.4(a) for the example case of a 10-fish school. The domain employed is $10c x 20c$, with the domain length growing for each longer school. Around the body, a fine mesh region is employed with a minimum grid spacing of 0.0035c. The resulting grid is 1696 x 704, giving about 1.2 million total grid points. The boundary conditions are also shown, with the velocity boundaries defined

by an inlet boundary condition with U_∞ from the left, an outlet boundary condition on the right to allow vortices to exit the domain without reflection, and zero gradient upper and lower boundaries with U_∞ to enforce free stream conditions. A grid independence study was completed on this grid, shown in Fig. 2.4(b). In the figure, the net-force in the -x direction is shown for the back fish using each of the grid sizings, where the coarse mesh has a minimum grid size of 0.0051c and the fine mesh has a minimum grid size of 0.0025c. The average and peak C_x values are within 2 percent for the nominal and fine grids, so the nominal grid is determined to be sufficient for the study.

2.5   Performance Definitions

To solve for the hydrodynamic forces, F_x and F_y, the solver directly integrates the projected surface pressure and shear force over each body. Thrust and drag are then computed by further separating the pressure and viscous stress components of F_x by their sign. The thrust on the body then consists of the sum of the forward force on the body, and the drag is the backward force on the body. The resulting force coefficients C_x, C_y, and C_T are computed by

$$C_i = \frac{F_i}{0.5\rho U_\infty^2 c}.$$
(2.4)

The total power is defined as the rate of the output work done by the fish to complete its motion. It is given mathematically by

$$P_u = \oint (-pn_i + \tau_{ij}n_j)\Delta u_i dS, \tag{2.5}$$

where n is the unit normal to the surface, and Δu_i is the velocity of the element dS relative to its surrounding fluid in the i-th direction. The coefficient of power can then be calculated as

$$C_{pw} = \frac{P_u}{0.5\rho U_\infty^3 c}. \tag{2.6}$$

From these coefficients, we define a modified Froude efficiency η consistent with previous studies [20], [34]:

$$\eta = \frac{U_\infty \overline{F_t}}{U_\infty \overline{F_t} + \overline{P_u}} = \frac{\overline{C_T}}{\overline{C_T} + \overline{C_{pw}}}. \tag{2.7}$$

where the overline ($\overline{}$) denotes values averaged over a cycle of motion.

For the study, parameters are selected to obtain a free-swimming condition for a single fish, such that the net force on the body is zero. To achieve this, the parameters are set to the values shown in Table I. A is a result of the equations given in Fig. 2.3. The chord length c and the frequency of the motion f are both set to one. The Reynolds number Re is initially chosen to be 1000. This is in keeping consistent with [20], [27],

corresponding to a higher Reynolds number in three dimensions [35], and keeps the

viscous effect small while still maintaining a coherent vortex structure [6]. The effect

of changing the Reynolds number is presented later in the study. Finally, the velocity

is varied to achieve the free-swimming condition. This results in a Strouhal number St

of 0.43.

Re	A	f	c	St	N_{fish}
1000, 2000, 4000	0.1	1.0	1.0	0.43	4, 7, 10, 13, 16, 19, 22, 23, 25

TABLE 2.1: Parameters used in this study

3 Hydrodynamic Interactions and Classification in a Large School

3.1 Arrangement of School

Biological studies have identified aerobic capacity, as well as anti-predator behavioral responses, essential in identifying unique spatial positioning groups of individual fish within a school [36], [37]. Despite some progress in understanding individual fish performance in 2-4 fish models, no significant understanding has been reached of how positioning within the school affects the hydrodynamic performance of the individual fish. This classification, along with the underlying hydrodynamics, are explored in this chapter.

To begin studying large fish schools, a baseline large school must be defined. Using the previously mentioned kinematics, the basic dense diamond school is used to determine the arrangement of the school. The diamond school shape has been identified by previous studies to be the most energy efficient for a small number of fish [1], [35], [38], and most recently the dense diamond school has been identified as the best-performing

diamond configuration [20]. To enable studies of a large number of fish in a school, we utilize the dense diamond as a basic sub-unit of the larger school. This allows us to observe the most efficient arrangements of fish. Additionally, the highly compact dense diamond maximizes interaction between fish within the school. Utilizing this configuration, we capture all of the fish-fish interactions experienced by schooling fish. In keeping with the findings of the previous study, the dense diamond is defined in Fig. 3.1 as $D = 0.4$ and $m = 0.4$. To construct larger schools, additional sub-units of the dense diamond are appended to the previous school. An example of adding length is shown in part (a), with one additional sub-unit shown in red. An additional example of adding width to the school is shown in part (b). In adding and subtracting sub-units, the overall length and width of the fish school are varied. To distinguish the fish within the school, fish are numbered top to bottom, left to right, as shown in Fig. 3.1(a). The notation f_a^b is used, where a is the fish number and b is the total number of fish in the school.
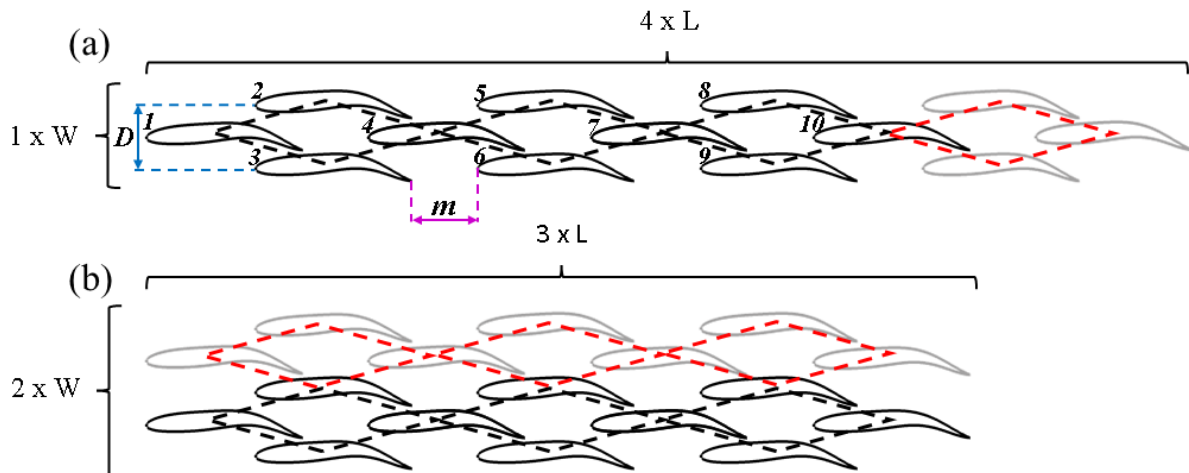

FIGURE 3.1: Arrangement of large schools based on dense diamond. Examples increasing length (a) and width (b) are shown.

3.2 Results

3.2.1 10 Fish School Hydrodynamics

To begin, a baseline school is studied, configured like a longer 4-fish school as shown in Fig. 2.3. The resulting cycle-averaged net force, along with the efficiency, thrust, and power consumption for individual fish, along with the school averages, are shown in Table 3.1. The performance of the school, in both C_x and η, is significantly higher than a single fish, with an average efficiency of 57.3%, a 30% improvement over the single fish swimming value of 44.2%, affirming that hydrodynamic benefit is gained by the fish through schooling. In comparing results with Pan and Dong [20], the larger school sees a continued efficiency benefit of 9% from schooling compared to the 4-fish dense diamond school.

	f_1^{10}	f_2^{10}	f_3^{10}	f_4^{10}	f_5^{10}	f_6^{10}	f_7^{10}	f_8^{10}	f_9^{10}	f_{10}^{10}	f_{avg}^{10}
$\overline{C_T}$	0.387	0.482	0.482	0.494	0.515	0.515	0.479	0.462	0.462	0.399	0.468
$\overline{C_{pw}}$	0.531	0.306	0.306	0.510	0.290	0.290	0.556	0.279	0.278	0.261	0.361
$\overline{C_x}$	0.067	0.090	0.090	0.13	0.084	0.084	0.100	0.047	0.048	0.085	0.083
η	0.421	0.612	0.612	0.492	0.639	0.639	0.463	0.623	0.624	0.605	0.573

TABLE 3.1: Cycle averaged performance in 10-fish school

In the individual fish data, efficiency is gained from schooling by every individual, with the least gain for f_1^{10} at the front of the school and the most gain for f_5^{10} and f_6^{10} in the middle. Symmetry in the cycle average performance is also seen across symmetric fish in the school, with f_2^{10} and f_3^{10}, f_5^{10} and f_6^{10}, and f_8^{10} and f_9^{10} having values within 1% of each other.
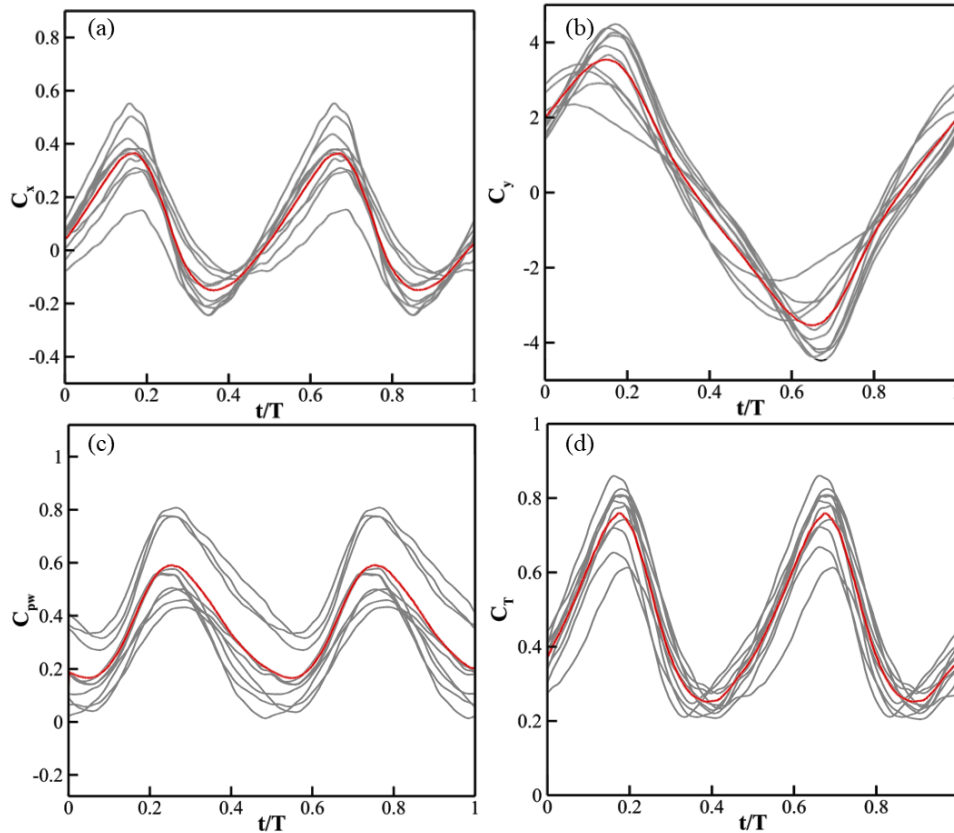
FIGURE 3.2: C_x (a), C_y (b), C_{pw} (c), and C_T (d) over a cycle of motion for every fish in the school, with the school averaged value shown in red.

Next, the force coefficients and power consumption are given in Fig. 3.2(a-d). Every individual fish is shown in grey, along with the school averaged values in red. From the figures, a 2-peak cycle is shown, with maximum C_T and C_y magnitudes occurring at $t/T = 0.2$ near the end of the left stroke, and again at $t/T = 0.7$ near the end of the right stroke of the tail.

To investigate the flow within the school the vorticity for the maximum and minimum C_x is given in Fig. 3.3. Major vortices for each group are labeled. To label individual vortices, $V^{\#}_{L/R,+/-}$ is used, where the top number indicates the fish where the vortex originates. The letter on the bottom indicates that it is generated during the left or
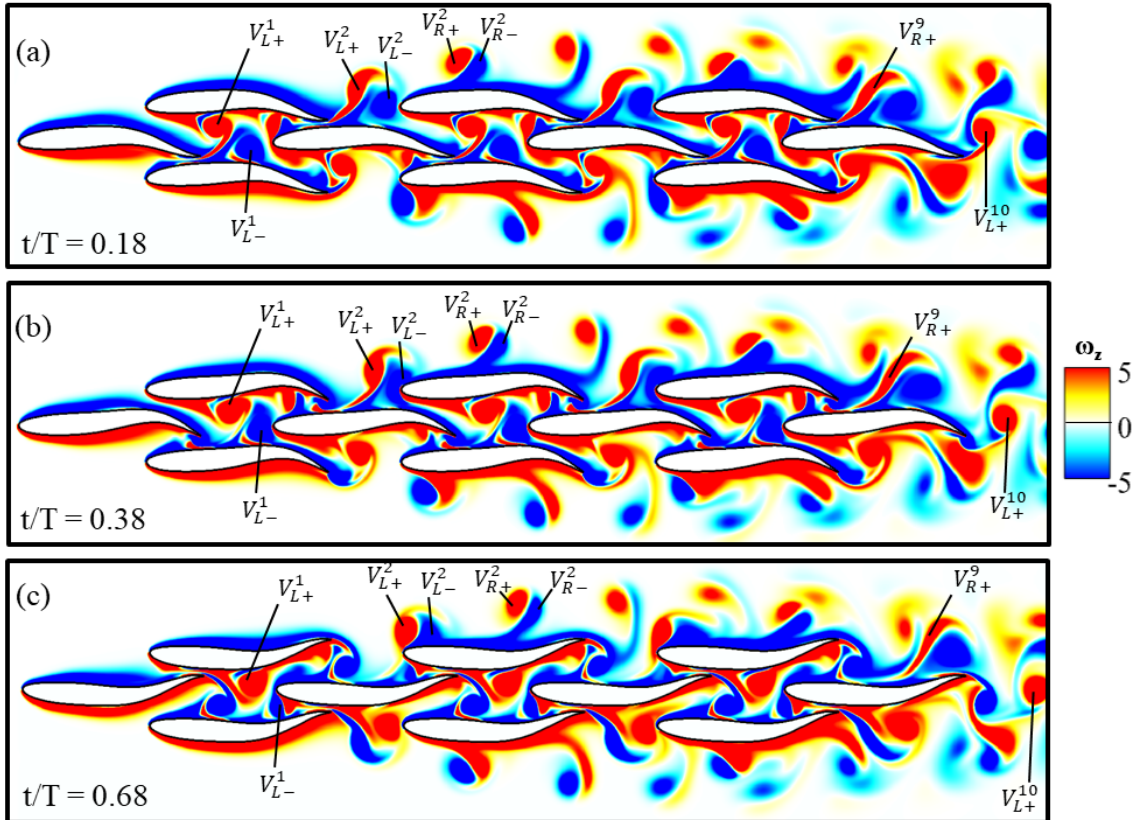
FIGURE 3.3: Vorticity (a-c) at $t/T = 0.18$, 0.68, and 0.38. Key vorticies are noted.

right stroke, and the plus or minus sign indicates the sign of the vortex, where positive vortices are counterclockwise and negative vortices are clockwise. During each half stroke, the leading-edge vortex is shed off the tail region of the fish. For all but f_{10}^{10}, the tail also interrupts the leading-edge vortex of the next fish in the school, causing the shedding of another vortex. The two shed vortices then advect downstream in a pair, as shown by V_{L+}^1 and V_{L-}^1. For the fish along the mid-line, the vortex pair is then captured by the channel of surrounding fish and intercepts the head of the next fish behind it. On the edges of the school, the pair advects laterally outside the school after intercepting the next fish in line, as shown by V_{R+}^2 and V_{R-}^2. For f_{10}^{10} at the back of the school, the lack of another fish to pull a leading-edge vortex off of gives a single vortex

$(V_{L+}^1, 0)$shed in each half stroke.

To summarize, the primary vortex structures are given in Fig. 3.4, with the major vortices represented along with the fish bodies. Each plot shows the major vortices relevant to the body shown in orange. First, f_1^{10} is characterized by no oncoming vortices to interact with and the vortices shed from the tail are contained completely by the channel created by f_2^{10} and f_3^{10} (a). Next, all the fish along the edges of the school are characterized by the lateral advection of the vortex pair shed at the tail, similar to the edge fish vortex pattern observed in the dense diamond school in Pan and Dong [20] (b). Apart from the front-edge fish, they have an incident vortex pair from the previous edge fish. Additionally, with the exception of the back-edge fish, there is another edge fish partially blocking the shed vortex from advecting in the streamwise direction. The fish along the midline of the school have a vortex pair from the previous fish interacting with its anterior, and the vortex pair it sheds is entirely constrained to the channel created by edge fish around it (c). The subsequent fish behind it blocks the streamwise advection of the vortex pair coming from its tail. Finally, f_{10}^{10} similarly has a vortex pair incoming from the channel in front of it, but behind it only generates a single vortex that is unobstructed as it flows downstream (d). Additionally, since there is no additional edge fish to disrupt the propagation of the vortex pair next to it, the pair coming from the neighboring back-edge fish also interacts with the tail portion of f_{10}^{10}.

The wake structure is shown in Fig. 3.5, with the major components labeled in the vorticity plot in (a) and the cycle averaged streamwise velocity in (b). The wake is shown to have a typical reverse Bérnard-von Kármán (rBvK) wake core behind f_{10}^{10},
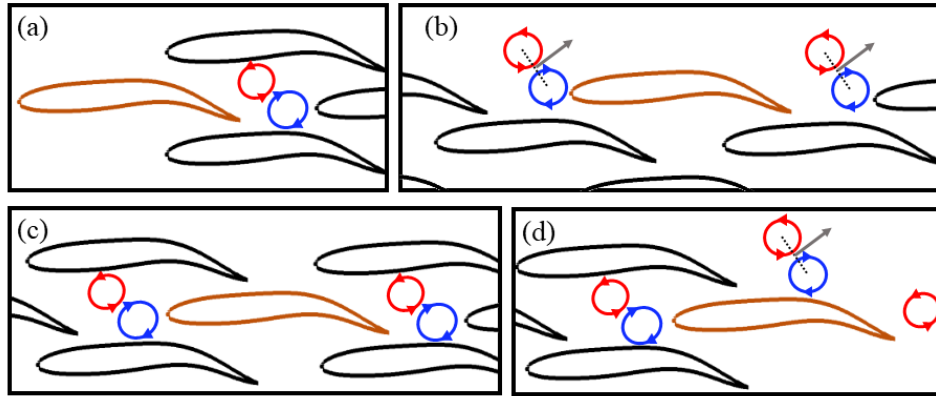
FIGURE 3.4: Schematic of primary vortex interactions based on arrangement of neighboring fish.

noted in black at the center of the wake. On the edges, two 2P wake pairs are observed in green, owing to the lateral proximity of f_8^{10} and f_9^{10} breaking the stability of the leading-edge vortex on f_{10}^{10} and creating a vortex pair. This overall structure matches the wake pattern shown by the dense diamond school in Pan and Dong [20], [21]. The additional vortices shed by the other fish along the edge of the school either combine with the wake structure present or are mostly dissipated before reaching the back of the school, creating a similar wake to the synchronous dense diamond school. The angle of the 2P vortex streets are more narrow than the 4-fish school results, owing to the weaker vortices from previous edge fish creating a channeling effect for the later vortex wake, trapping it in a more narrow space as can be seen in V_{R+}^9 in Fig. 3.3. Additionally, the lateral spacing between the positive and negative vortices in the rBvK wake is wider than the in-phase diamond school of [21], which notes that the wider spacing generally correlates with higher C_x in the school. In the cycle averaged velocity (b), small but increasing jets are observed along the edge of the school, originating from an edge fish and occurring along the subsequent fish body. Behind the school, a

single narrow long jet is observed, correlating with the rBvK wake in the vortex wake. Additionally, two short jets occur behind the edges of the school, corresponding to the 2P vortex structures discussed previously.
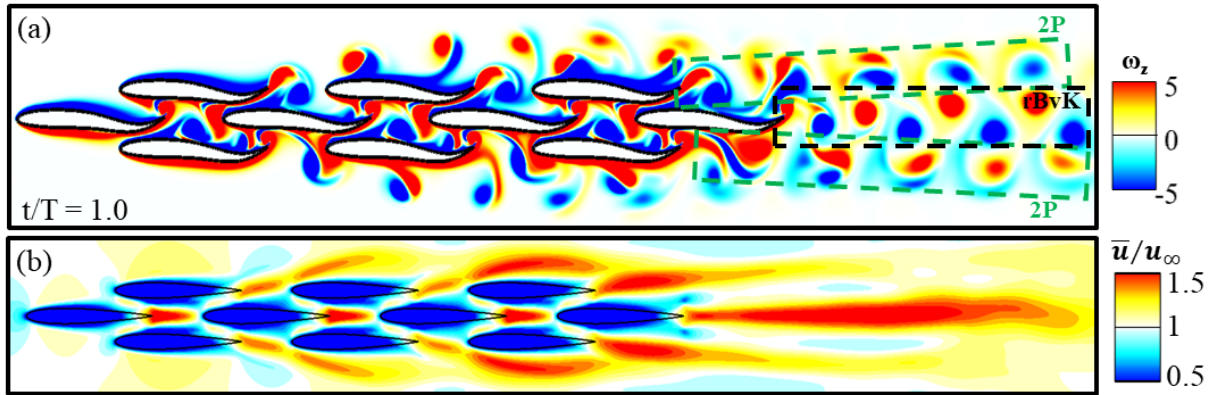
FIGURE 3.5: Vorticity (a) and time averaged velocity (b) demonstrating the wake structure in the 10-fish school.

Next, the force vectors are plotted along the surface of each fish body at the peak thrust of $t = 9.18T$ in Fig. 3.6(a). The forces with a net thrust production are shown in red, and the net drag production is shown in blue. From the figure, a surprising result is seen amongst many of the fish. In addition to the expected higher thrust output near the tail, all except the front and top edge fish have suction thrust on the head portion of the body. For example, a drag-producing region is observed on the front half of the top of all edge fish along the top of the school ($f_2^{10}, f_5^{10}, f_8^{10}$) whereas all other fish have some thrust production in that region. On the same fish, there is a high thrust region on the top of the tail portion that also occurs only in f_{10}^{10}. The front half of f_{10}^{10} has the same pattern as the middle fish, f_4^{10} and f_7^{10} with a high thrust region in the front followed by a drag-producing region around the middle. The bottom-edge fish have a large thrust-producing region in the first half of the top edge. For the edge fish, the top

and bottom are different because they are in different parts of the cycle, with the top

edge tail flapping in towards the middle of the school and the bottom edge tail flapping

away from the middle of the school. The top edge is in peak tail thrust production at

$t/T = 0.18$, while the bottom edge is in peak head thrust production corresponding to

$t/T = 0.68$ in the figure. The school shape is symmetric, however, so the bottom edge

fish experience the tail and head thrust production times opposite of the top edge fish.

The opposite can be seen at $t = 9.68T$ in part (b). At this time, the top edge has suction

force at the head, and the bottom edge has a larger net thrust at the tail. The fish along

the mid-line have a mirrored performance to $t = 9.18T$.
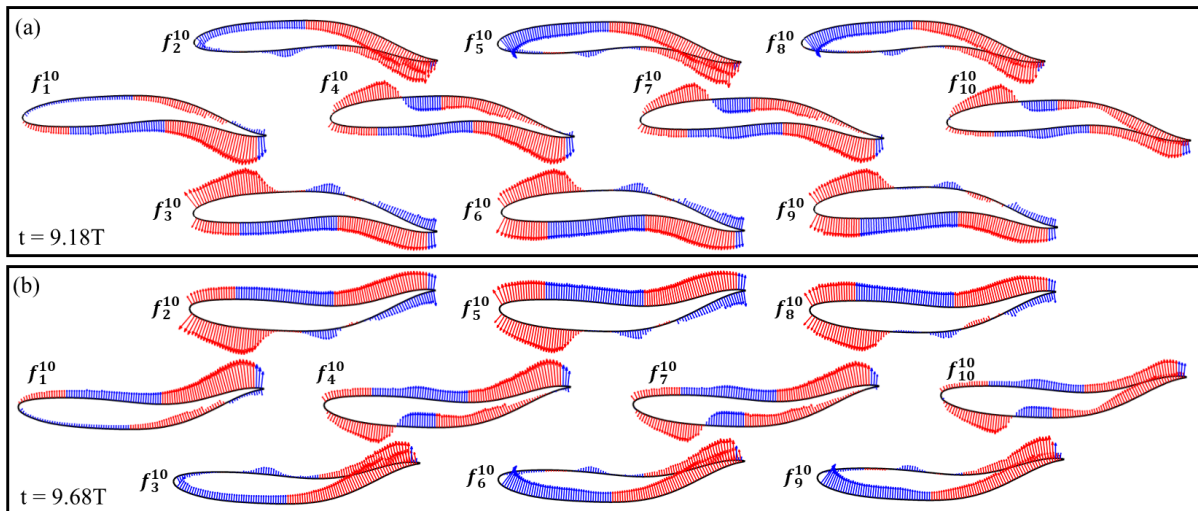
FIGURE 3.6: Surface force vectors along each fish in the 10-fish school at the peak thrust production, $t/T = 0.18$ (a) and $t/T = 0.68$. Blue denotes net drag, and red denotes net thrust on the surface.

Next, the spatiotemporal force ($F_x = -(-pn_x + \tau_{xi}n_i)$) for each fish in the school is

shown in Fig. 3.7. The overall pattern of two zones of high thrust near the tail, shown

in red, corresponding to the end of the left and right strokes, is consistent with the

previous study of Pan et. al [21]. As expected, the front half of the front fish f_1^{10} shows

unique performance, with a consistent drag zone on the tip through the entire cycle (a). The back half of the front fish, however, is very similar to the other mid-line fish (f_4^{10}, f_7^{10}, f_{10}^{10}), with two consistent zones of high thrust near the back. The subsequent mid-line fish also have a smaller thrust zone near the head twice each cycle. The back fish has a smaller high thrust zone during its two peaks. Most unique is the fish along the edge of the school (f_2^{10}, f_3^{10}, f_5^{10}, f_6^{10}, f_8^{10}, f_9^{10}) which have a single high thrust and single high drag phase on the front, with a very high magnitude of each. Additionally, unlike the 2 high thrust regions on the back observed by all other fish, there is only one region of high thrust. The high thrust on the tail occurs when the tail is flapping inwards towards the school, and the performance for symmetric fish ($f_{2/3}^{10}$, $f_{5/6}^{10}$, and $f_{8/9}^{10}$) is similar, with the half cycled performances flipped.
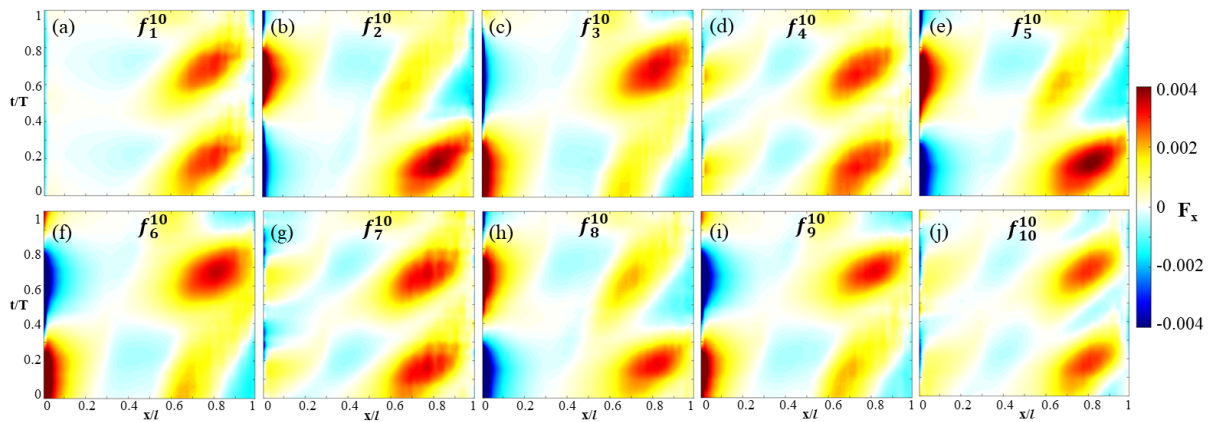
FIGURE 3.7: Spatiotemporal forward force $F_x = -(-pn_x + \tau_{xi}n_i)$ along the fish body through one cycle of motion for each individual in the school.

The spatiotemporal power consumption $Pw = -(\bar{\sigma} \cdot n) \cdot u)$ for each fish in the school is shown in Fig. 3.8. The overall pattern of two zones of high power consumption near the tail, shown in red, corresponding to the end of the left and right strokes, is consistent with the previous study of Pan et. al [21]. While more consistent than force, there

are still significant differences in power consumption between individual fish. First, the fish along the edge of the school has one small and one large power consumption zone near the tail, with the smaller and larger zone corresponding to the tail flapping away from and towards the school, respectively. Additionally, the back fish, f_{10}^{10} has smaller high power consumption regions for both the left and right stroke.
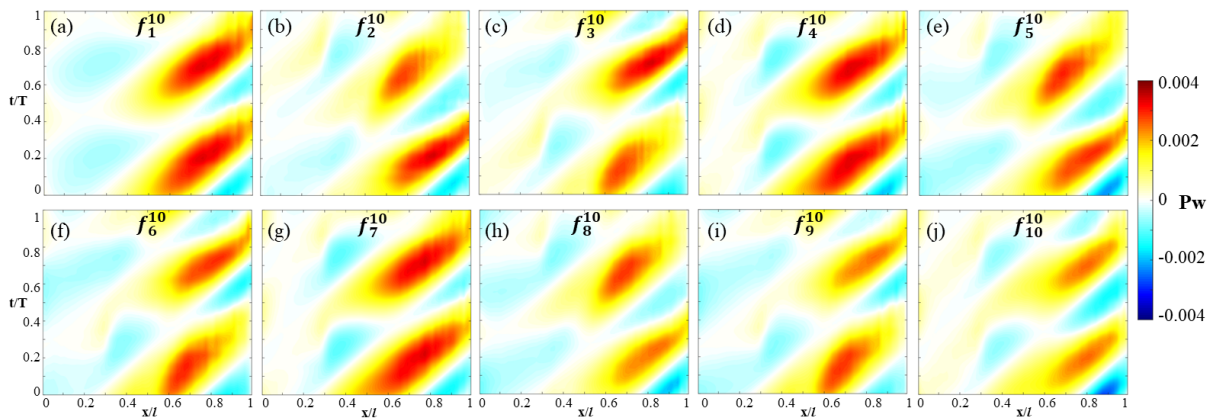
FIGURE 3.8: Spatiotemporal power consumed $Pw = -(\bar{\bar{\sigma}} \cdot n) \cdot u$ along the fish body through one cycle of motion for each individual in the school.

3.2.2 Anterior Body Suction

Next, the body-body interactions are studied in detail. From the works of Pan and Dong [20], [21], a few primary body-body interactions within the dense diamond school have been discussed. Within the dense diamond study, the block effect, wall effect, and anterior body suction effect are shown to be dominant body-body interactions in determining the performance of the individual fish in the school.

To begin, the anterior body suction effect is investigated in detail. This effect is shown in Pan and Dong [21] to occur from the low-pressure suction that is generated on the tail of one fish interacting with the head of the fish behind it. In the paper, the effect

is discussed within the context of the back fish of the diamond, which saw a moderate suction force on its head when the body phases are matched. To investigate the effects of this throughout the school, the anterior portion of the body, defined as the first 30% of the body length, is observed through the cycle of motion. The net force is plotted in Fig. 3.9, with the superscript a denoting the anterior portion of the body only. Note that only the top edge fish are included in the figure, as it has already been shown that the bottom-edge have the same results due to symmetry. Additionally, the pressure contour is shown at $t/T = 0.25$(a) and $t/T = 0.75$(b). The mid-line fish all show 2 peaks and 2 troughs in f_x^a, whereas the fish along the edge of the school have a single peak and trough of significantly higher magnitude.

The reason for this can be seen in Fig. 3.9(a). In this time step, the top-edge fish are experiencing peak thrust from the anterior body suction. The bottom-edge fish, on the other hand, are near the lowest point in their anterior net force. This can be seen using the example of the front fish (f_1^{10}). The front fish tail has created a low-pressure suction and high-pressure pushing on each side of its tail. On the suction side, the top-edge fish (f_2^{10}) is benefiting heavily from interacting with this low-pressure suction zone, gaining a large net forward force on its anterior. On the other side, however, the high-pressure side of the front fish also interacts with f_3^{10}, creating a large drag on its anterior portion. This effect also explains the high-thrust zones at the head seen in Fig. 3.7 where the mid-line fish have two small thrust and drag zones and the edge fish has one large thrust zone and one large drag zone on its anterior. This effect can be seen all along the edge fish on the top and bottom of the school in Fig. 3.9(a) and is
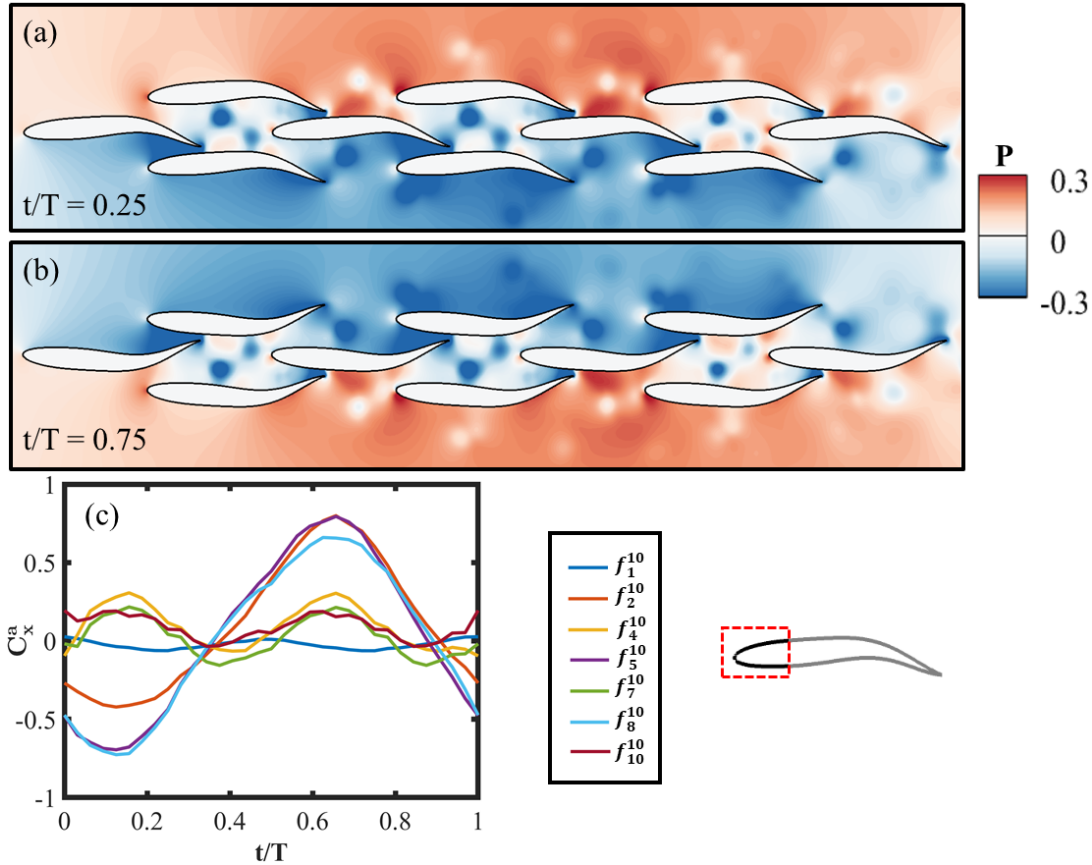
FIGURE 3.9: Anterior body suction effect shown using a pressure contour (a-b) and anterior net force (c) over a cycle of motion for each fish. Anterior fish body is defined as the first 30% of the body, as shown.

expected to occur any time the suction side of a tail is near the head of another fish. In the middle fish, some net suction on the anterior is still observed, similar to the back fish here and in prior work [21]. This occurs due to similar suction and pushing as the edge fish, but because it has a fish on either side of it, the effects occur simultaneously. The low and high-pressure regions on the anterior largely cancel out, leading to a much smaller net effect. The net effect is still suction on the anterior because the low-pressure tail is much nearer to the head of the fish than the high-pressure tail. This allows the low-pressure zone to be more dominant around the anterior, leading to the smaller net suction observed in the middle and back fish. An example of this is seen in Fig.

3.9(a), where f_4^{10} has mostly low-pressure around its head but is not as dominant as the previously discussed edge fish. The low-pressure from f_3^{10} and high-pressure from f_2^{10} are largely canceling out, but the head of f_4^{10} is significantly closer to the tail of f_3^{10}, meaning the low-pressure is more dominant on the body. The results of this suction can be seen in Fig. 3.6. In the figure, the mid-line fish are all experiencing moderate anterior body suction, focused around the top-edge of the fish. The bottom-edge fish are in a high anterior body suction state with high net force around the head, and the top-edge fish are in the opposite state, with high drag around the head resulting from high-pressure in front of them. Throughout this motion, the power consumption remains similar between groups on the anterior, but the front and edge fish consume less than the middle and back. Because of this, the edge fish have a more distinct cycle of high and low net force on the anterior. One when the tail is flapping into the school where the anterior is low net force, and subsequently low efficiency, and another where the tail is flapping away from the school, where the net force is high and the power consumption has not significantly increased, so the efficiency is significantly higher.

3.2.3   Block Effect

The block effect is shown in Pan and Dong [20] to occur when the flow behind a fish body is blocked by another body, leading to an increase in pressure between the fish and increasing the performance of the front fish. In the context of their dense diamond school, it was demonstrated in the front fish when adding the back fish to the school, with the channel of edge fish present to block the flow from propagating laterally. Also,

it is shown that blocking the flow of the vortices and preventing the formation of the downstream jet behind the front fish lead to the benefits of the block effect. Within the context of the large school, the block effect is also observed. From the observations of the vortex structure in Fig. 3.3, we know that the vortices behind f_1^{10}, f_4^{10}, and f_7^{10} are blocked in their downstream propagation and f_2^{10}, f_3^{10}, f_5^{10}, and f_6^{10} also have partial blocking of the vortex pairs from the downstream.
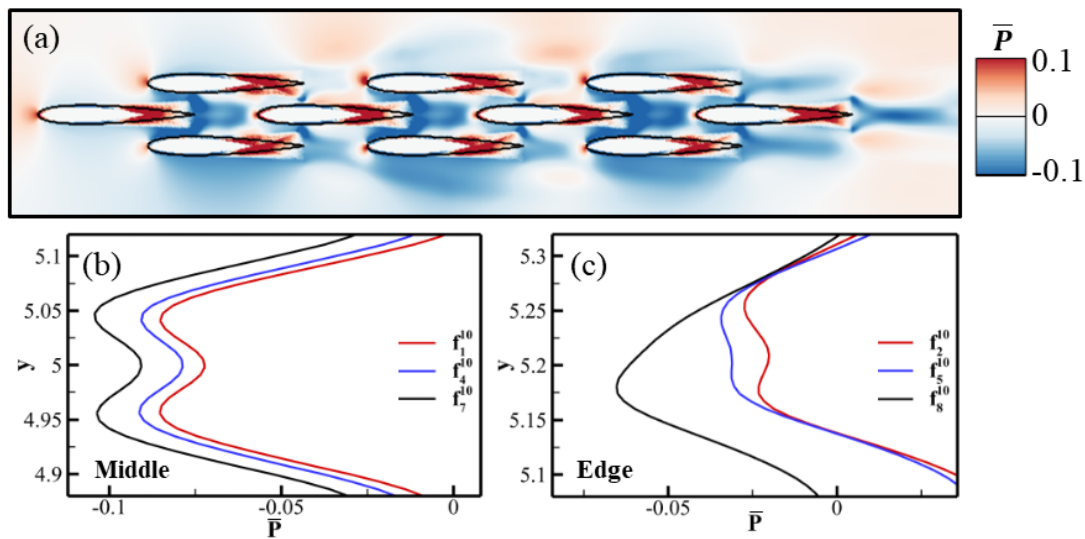
FIGURE 3.10: Demonstration of the block effect utilizing the cycle-averaged pressure (a). The cycle averaged pressure profile at $0.1l$ behind each fish tail for the mid-line fish (b) and top-edge (c) fish are also shown.

To investigate the effects further, the cycle-averaged x-velocity is shown in Fig. 3.5(b), and the cycle-averaged pressure distribution is given in Fig. 3.10(a). From the figure, a similar but stronger jet arrangement is shown compared to the dense diamond. The edge fish, except the back-edge, only see a small momentum-carrying jet behind them, and a larger one occurs at the head of the next edge fish, owing to the partial blocking of the flow by the next edge fish. This corresponds with a higher pressure than is observed behind the fish, observed in Fig. 3.10(a), giving further evidence of the presence

of a partial block effect occurring along the edge of the school. Additionally, the same interrupted pressure zone shape observed in Pan and Dong [20] is observed in the channel behind the front and middle fish. Unsurprisingly, the block effect continues to occur in the channel for each of these fish. Unexpectedly, however, the higher pressure behind the fish due to another fish behind it within the channel is not limited to a single fish in the channel behind. This is shown more clearly in Fig. 3.10(b-c), which shows the cycle averaged pressure profile at $0.1l$ behind each fish along the mid-line and top edge of the school. The pressure continues to raise going from the back of f_7^{10} to f_4^{10} to f_1^{10}. This can be explained by the further blocking of the fluid flowing down the channel. For f_4^{10}, there is both f_7^{10} and f_{10}^{10} in the channel behind it, leading to a further increase in pressure compared to just one fish blocking the flow. This enhanced block effect is observed along the middle channel, but also in a much weaker form for the edge fish, where the pressure behind f_2^{10} is increased slightly compared to f_5^{10} because of the presence of more fish behind it. The effect of this is significantly lessened, however, because of the lack of a channel containing the flow, so much of the fluid flows laterally around the subsequent blocking fish, as seen in the jets of Fig. 3.5.

3.2.4 Wall Effect

Finally, previous studies from Quinn et al. [39], [40] have shown that foils oscillating near a solid boundary lead to a 40% increase in thrust at 0.4 chord length from the wall, with only a slight increase in power consumption. Additionally, this effect was observed in Pan and Dong [20] for a dense diamond fish school, with the tail edge of

the fish breaking the stability of the leading-edge vortex on the "wall" fish. The same

pattern of vortex pairs shedding reported by Pan is seen in the flow behind edge fish

within the 10-fish school. This is shown along the edge of the school in Fig. 3.3(a),

where the vortex pair V_{L+}^2 and V_{L-}^2 are very similar to the flow structure of the wall

effect in the dense diamond reported previously. The basic wall effect occurs any time

the tail of a fish flaps close enough to the body of another fish for the fish body to

create the effect of a "wall" near the tail of the previous fish. This occurs during half of

the strokes for fish along the edge of the school, and both strokes along the mid-line,

except f_{10}^{10}. Along the edge, the wall effect only occurs when the tail flaps towards

the center of the school. By flapping near a wall, the lateral momentum generated

by the tail motion is redirected by the wall downstream. To demonstrate this effect,

the normalized x-velocity is shown in Fig. 3.11(a). At this time step, the bottom-edge

fish are flapping away from the school and the top edge fish are flapping towards the

school. From this, we expect the top-edge fish to experience a wall effect while the

bottom-edge fish does not. This is evident from the velocity zones behind each of the

fish, where the top edge fish has a temporary jet of fluid flow downstream, indicating

high momentum gained by the fish via Newton's third law. The bottom fish, on the

other hand, has no high momentum region.

To compare wall effects among the fish, the total momentum of the instantaneous jet

behind the tail is summed, and the results are given in Fig. 3.11. From the figure, the

fish without any wall effect (f_3^{10}, f_6^{10}, f_9^{10}, and f_{10}^{10}) have significantly less momentum at

the tail. As expected, the top edge fish (f_2^{10}, f_5^{10}, and f_8^{10}) have the highest momentum,
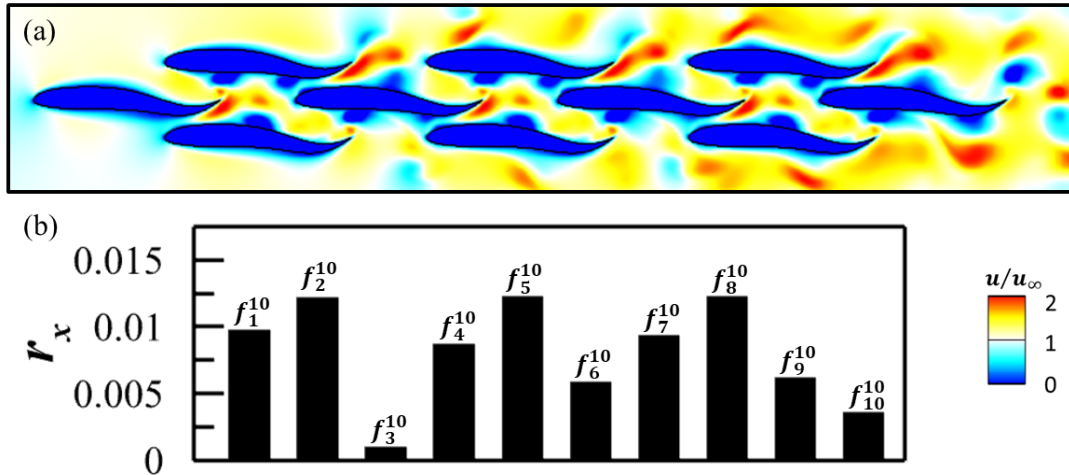
FIGURE 3.11: Normalized x-velocity (a) in the 10-fish school at $t/T = 1.0$, along with the total streamwise momentum in the temporary jet formed behind each fish (b).

and the fish with smaller momentum jets due to blockage from the middle channel (f_1^{10}, f_4^{10}, f_7^{10}). The discrepancy between the top and bottom edge fish explains the single high thrust region on the edge fish tail observed in Fig. 3.7, while all the other groups had 2 zones of similar thrust at the tail. Behind the front (f_1^{10}) and middle (f_4^{10}) fish with similar high-momentum jets are observed, however, they are interrupted by the subsequent body inside the channel. Because of this, the benefit from the wall effect is lessened for these front and middle fish compared to the edge fish. This explains the weaker thrust region for all but the edge fish observed in Fig. 3.7.

3.2.5 Classification of Individual Fish

All the hydrodynamic interactions between swimmers and their wakes are based on the spatial arrangement of neighboring fish. Because of this, the fish within the large school can be grouped based on the arrangement of nearby fish. The resulting classification and grouped results are shown in Fig. 3.12. In part (a), $\overline{C_x}$ is plotted against

η, and distinct groups of individual fish performance emerge. Specifically, there is a region of multiple high-efficiency fish and a region of higher net force fish. In referencing the geometric positions within the school, groupings are indicated by the results. First, the front fish have no other fish in front of it to benefit from, so they have the lowest performance in both η and $\overline{C_x}$, but the $\overline{C_x}$ value is still improved over a solo swimmer due to the block effect. Next, the edge fish have fish on only one side of them and experience a unique anterior body suction and wall effect. They occupy the highest η region circled in blue, with about a 46% improvement over the front fish. The $\overline{C_x}$ value is around the average for the school. The edge group is further broken down into front-edge, shown in blue, and back-edge, shown in purple. This distinguishes edge fish that have no incident vortices (front-edge) and no block effect (back-edge) from the others. Because of this, the front-edge fish have a lower η, and the back-edge fish have a lower $\overline{C_x}$. Despite this, the edge fish are overall similar and can be combined into a larger group. The middle fish are surrounded by other fish in the school, experiencing full anterior body suction, wall effect, and block effect within the entirety of the group. They show a consistent improvement in $\overline{C_x}$ of about 70% compared to the front fish, but the efficiency of the middle group is lower than the average of the school by about 20%. Finally, the back fish has no other fish behind it, experiencing only anterior body suction, and has about a 50% improvement in η compared to a single fish.

Fig. 3.12(c-f) show the force coefficients and power consumption. They are averaged within each of the spatially motivated groups, and the standard deviations are given by the shaded region. The standard deviation and average for the edge fish show only the
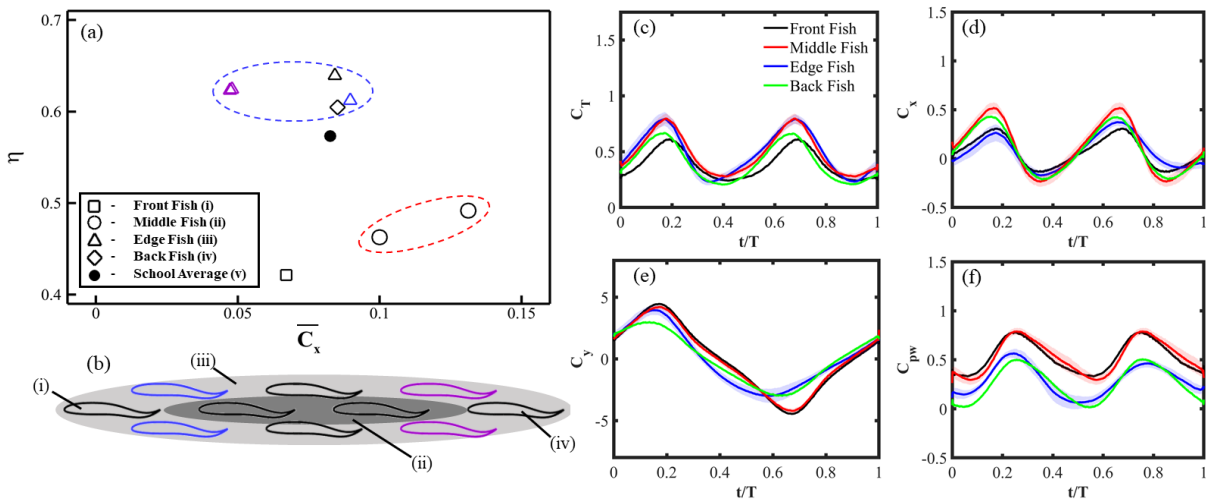
FIGURE 3.12: (a) Cycle-average force coefficient vs. efficiency in the school by group. (b) Arrangement of baseline school groups, with (i) front fish, (ii) edge fish region, (iii) middle fish region, and (iv) back fish definitions. Front-edge fish (blue) and back-edge fish (purple) are also denoted. C_T (c), C_x (d), C_y (e), and C_{pw} (f) are shown over a cycle of motion. The average for each group is plotted along with the standard deviation for the group. Only the top edge fish are included for the edge fish.

top edge fish, as the bottom edge is a mirror opposite of the top edge. The plots overall show unique and distinctive performance trends within each spatially motivated group. By showing similar trends over a cycle within each group, it is demonstrated that the common fish-fish interaction mechanisms taking place within each group lead to similar performance trends within the group. With these plots, many observations can be made that correspond to the performance groups shown in Fig. 3.12(a).

First, the front fish, shown in black, demonstrates the lowest C_T (c) and C_x (d), while both the horizontal force C_y (e) and the power consumption C_{Pw} (f) are highest for the front fish, which tracks almost exactly as a middle fish. Next, the edge fish, shown in blue, has the highest C_T (c), along with the middle fish, but has a significantly lower

C_x (d) compared to the edge and back fish. Interestingly, the peak in C_T is approximately equal in the left and right strokes, however, the right stroke has a higher peak C_x ($t/T = 0.7$) while the left stroke has a higher peak C_y ($t/T = 0.2$). The stroke generating significantly less horizontal force is also slightly higher in net force production, due to the anterior body suction. The power consumption is less throughout the entire cycle compared to the middle and front fish and is lower during the right stroke peak as the tail flaps away from the school than the left. The largest values in C_T (c), C_x (d), and C_y (e) are the middle fish. Subsequently, the power consumption (f) is also highest for the middle fish. Finally, the back fish, shown in green, has a lower C_T (a) than the front and middle, but still maintains a net force near the middle fish values, significantly higher than the edge fish. The lateral forces C_y (d) are significantly lower than other groups, and the power consumption is also lower than the others.

3.2.6 Effect of Reynolds Number

Arrangement	$\overline{C_T}$	$\overline{C_{pw}}$	$\overline{C_x}$	η
Re = 1000				
Single Fish	0.218	0.275	0.00	0.442
10-Fish School Average	0.468	0.361	0.083	0.573
Re = 2000				
Single Fish	0.209	0.242	0.044	0.464
10-Fish School Average	0.427	0.297	0.086	0.603
Re = 4000				
Single Fish	0.207	0.225	0.070	0.479
10-Fish School Average	0.404	0.257	0.087	0.624

TABLE 3.2: Reynolds number effect on school average performance

Next, the hydrodynamic interactions and proposed categorization is tested with a variety of Reynolds numbers to observe sensitivity to flow parameters. Note that lower

Reynolds numbers in 2D correspond to higher ones in 3D [20], [35]. For this, a single fish and 10-fish school are used, and the Reynolds number increases from 1000 to 2000 and 4000. The school-averaged results are given in Table 3.2. In the table, a general trend of decreasing thrust while also decreasing power as the Reynolds number increases is seen. This results in a slight increase in efficiency at higher Re, however, the benefit over a single fish from schooling maintains a 30% efficiency gain regardless of the change.
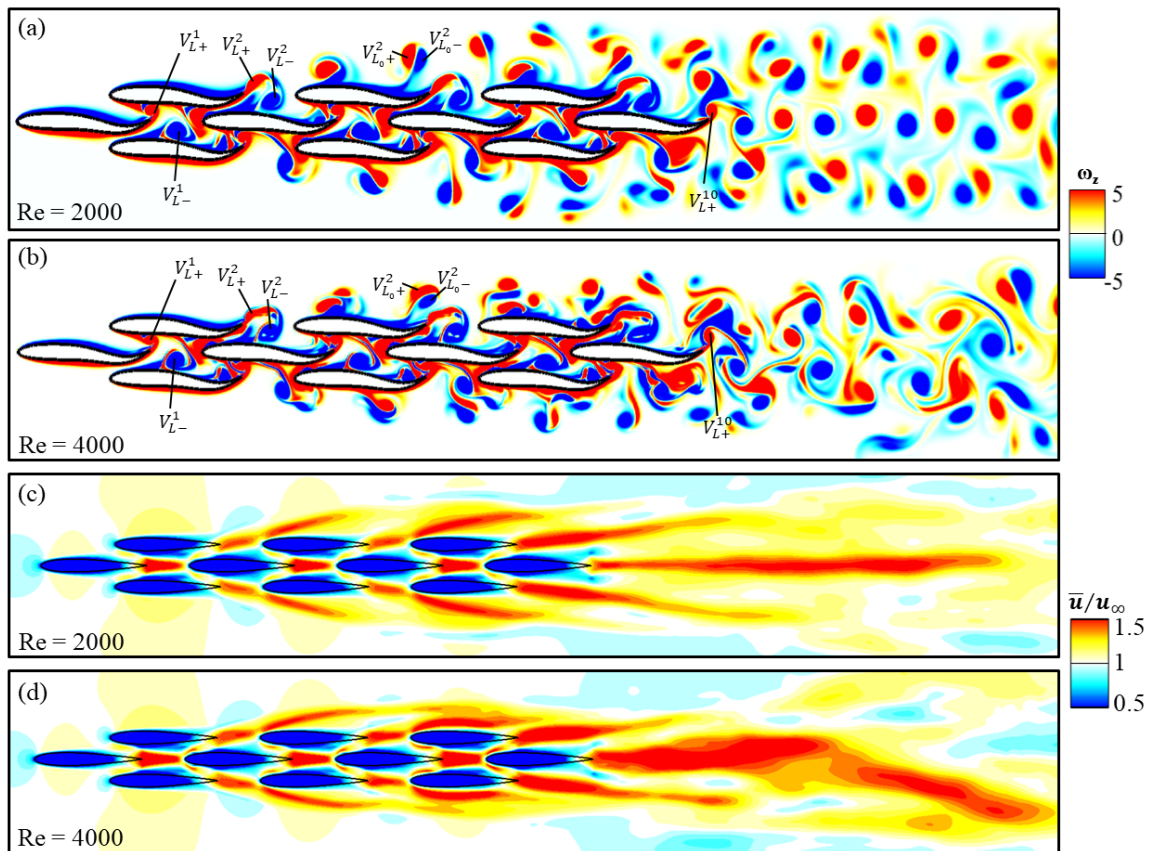

FIGURE 3.13: Vorticity at the peak thrust production (t = 9.18T) for $Re = 2000$ (a) and $Re = 4000$ (b), and cycle averaged streamwise velocity (c-d).

Next, the vorticity (a-b) and cycle averaged streamwise velocity (c-d) for the increased

Reynolds number is shown in Fig. 3.13. Overall, the cohesiveness of the vortex struc-

tures in the wake declines as the Reynolds number increases. Specific structures in the

flow are observed and compared with similar features in Fig. 3.3. In the front, middle,

and back fish, the same vortex pair trapped inside the channel is observed in V_{L+}^1 and

V_{L-}^1 at all 3 Reynolds numbers. Because they are fully contained by the channel, there

is little opportunity for any change in behavior of the vortex pair. In the back fish, the

same single vortex V_{L+}^{10} is generated, however, it has constructive interaction with the

preceding back-edge fish vortex pair V_{R+}^9 at increasing Reynolds number, where there

was previously no interaction between the two. Finally, the edge fish has a similar

vortex pair V_{L+}^2 and V_{L-}^2 that is shed from one edge fish and partially interacts with

subsequent edge fish for all Reynolds numbers. The cohesiveness of the pair declines

significantly at increased Reynolds numbers, however, it is still distinct and has clear

interaction with the subsequent edge fish. One major difference comes in the prop-

agation of the edge vortex pair beyond its interaction with the tip of the next edge

fish. At the lower Reynolds numbers, the pair propagates laterally into the free stream

beside the school, with minimal interaction between the vortex cores and any subse-

quent body or vortex structure. In the higher Reynolds numbers tested, however, the

pair has better adhesion to the body after interacting with the leading-edge, and sub-

sequently interrupts the generation of the next pair, contributing further to the decline

in the cohesiveness of the vortex structure. This is demonstrated by V_{L0+}^2 and V_{L0-}^2,

which originated at f_2^{10} during the previous left stroke. It is seen in Fig. 3.13 interrupt-

ing the propagation of V_{L+}^5 and V_{L-}^5 downstream. Despite the minor differences, the

schematic of primary vortex structures around the body given in Fig. 3.4 is consistent

at the higher Reynolds numbers studied. In comparing the wakes, at $Re = 2000$ there is more lateral deflection from the wall effect than the baseline, creating a second 2P pair from $f_{5/6}^{10}$ in addition to the 2P pair from $f_{8/9}^{10}$. The short jets behind edge fish diverge more from the center of the school and are longer than the baseline. The long middle jet is narrower, as the lateral spacing between vortices in the rBvK vortex street in the center is reduced. At $Re = 4000$, the wake is narrowed and lacks a consistent coherent structure. The short jets along the edges of the school are similarly longer but directed more in the streamwise direction contrary to $Re = 2000$. Additionally, the long center jet is significantly wider and deflects downwards.
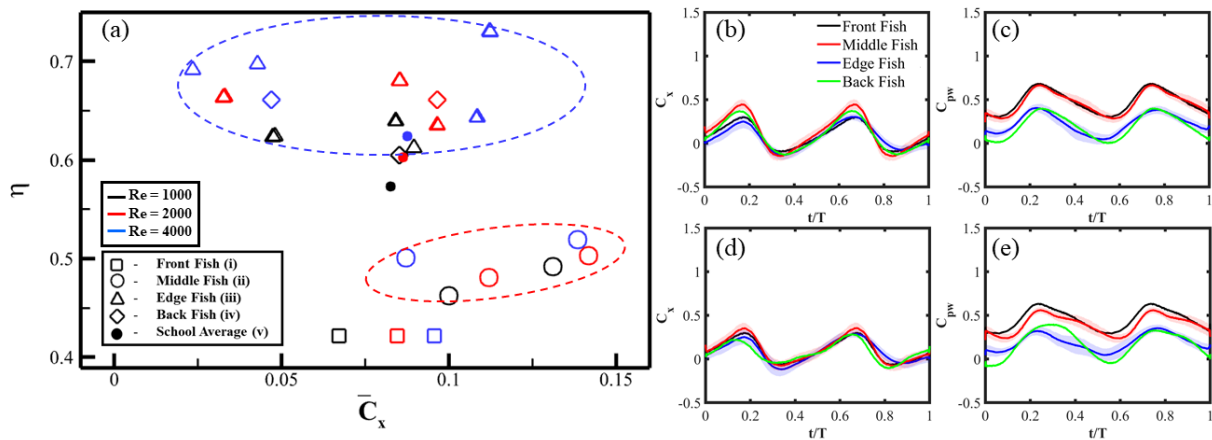

FIGURE 3.14: (a) $\overline{C_x}$ plotted with η for the groupings of a 10-fish school with Reynolds numbers 1000, 2000, and 4000. C_x (b,d) and C_{Pw} (c,e) over a cycle of motion by group, with the standard deviation for the group shaded for $Re = 2000$ (b,c) and $Re = 4000$ (d,e). Only the top-edge fish are considered in the average and standard deviation.

Finally, the results from utilizing the previously defined groupings are shown in Fig. 3.14. Once again, the higher η edge fish and higher C_x middle fish zones are immediately apparent at all 3 Reynolds numbers. The range of values within a group grows with the increase in Reynolds number, even as the groups remain distinct from each

other. The back fish are high η and the front fish is the lowest η at all 3 Reynolds numbers. In the body-averaged values, the standard deviations increase slightly with each increase in Reynolds number. This makes sense, as the vortex structures become less coherent at higher Reynolds numbers the consistency within each group will start to decrease. Additionally, the values for C_x get closer together with each Reynolds number increase. This comes from less constructive vortex-body interactions resulting from less coherent vortex structures. Also, the increase in a single fish net thrust is anticipated from the previous results from Khalid et al. [28], increasing the C_x of lower-performing front fish. Despite this, the groups remain distinct from each other, especially in power consumption. At higher Reynolds numbers, the same overall trends are seen as the 1000 Reynolds number baseline. Overall, the groupings are shown to be robust with respect to Reynolds number. Despite small changes in vortex wakes, the wall effect, block effect, and anterior body suction all remain and are caused by the spatial arrangement of neighboring fish.

3.2.7   Effect of School Length

$\overline{C_T}$	$\overline{C_{pw}}$	$\overline{C_x}$	η
0.537	0.396	0.081	0.583

TABLE 3.3: School average performance of 16-fish long school.

Next, the effect of making the school longer is examined by adding two more dense diamond units to the end of the school, resulting in a 16-fish long school. The school-averaged results are shown in Fig. 3.3. Compared to the 10-fish school, there is an increase in both average thrust production and power consumption, resulting in a slight

increase in net efficiency. The vorticity and cycle averaged streamwise velocity are shown in Fig. 3.15. The wake behind the school has a wider rBvK vortex street and a corresponding wider long jet in the center. The small jets resulting from the edge fish continue to strengthen as the school gets longer, ending in stronger short jets at the 2P vortex pairs on the edge of the school. In the near-body vortices, the front, middle, and back fish, the same vortex pair trapped inside the channel is observed in V_{L+}^1 and V_{L-}^1. Because they are fully contained by the channel, there is little opportunity for any change in the behavior of the vortex pair. In the back fish, the same single vortex V_{L+}^{16} is generated. Finally, the edge fish has a similar vortex pair V_{L+}^3 and V_{L-}^3 that is shed from one edge fish and partially interacts with subsequent edge fish.
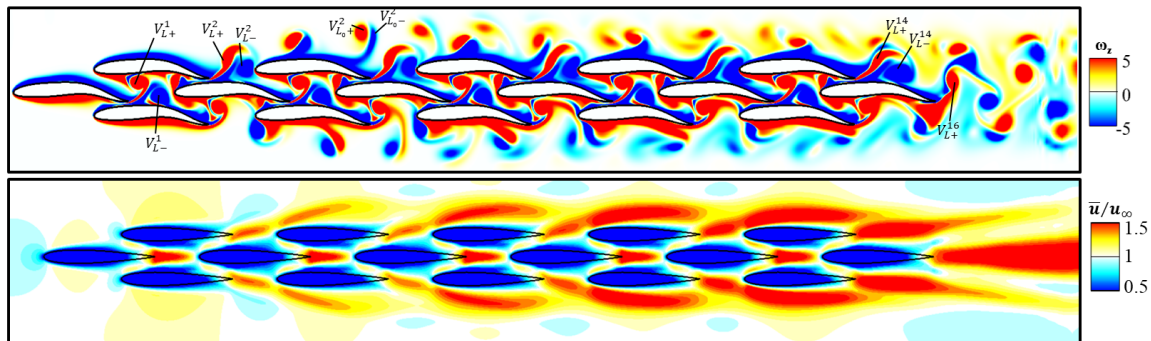

FIGURE 3.15: Vorticity at $t/T = 0.18$ (a) and cycle averaged streamwise velocity (b) in the 16-fish long school.

Finally, the longer school is grouped similarly, and the results are shown in Fig. 3.16. The same zones of high efficiency and high net force from the edge and middle, respectively, are observed in part (a). The overall spread among C_x in the edge fish is larger, with a bigger drop for the back edge fish than the 10-fish school. In the continuous coefficients of net force and power (c-d), the same patterns emerge, with middle fish having the highest net forces and power consumption throughout the cycle.
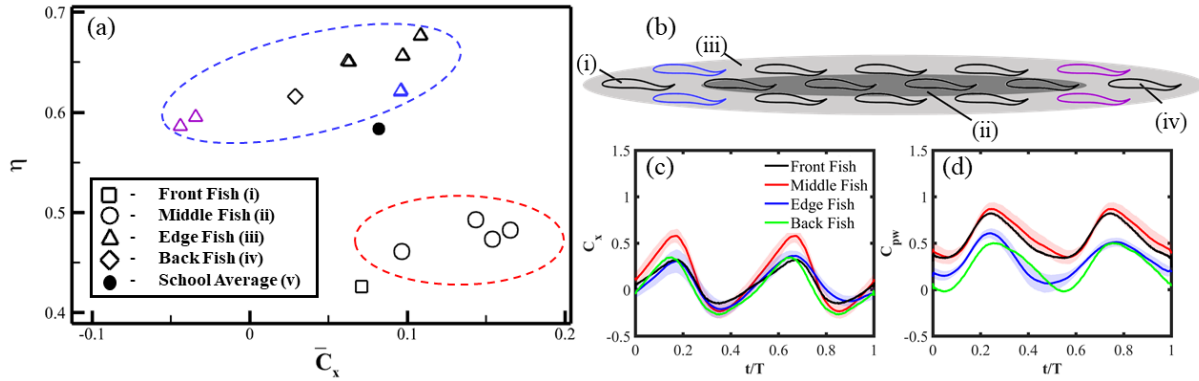
FIGURE 3.16: $\overline{C_x}$ plotted with η for the 16-fish long school (a). Schematic of groupings and arrangement of school (b). C_x (c) and C_{Pw} (d) over a cycle of motion by group, with the standard deviation for the group shaded. Only the top-edge fish are considered in the average and standard deviation.

3.2.8 Effect of School Width

$\overline{C_T}$	$\overline{C_{pw}}$	$\overline{C_x}$	η
0.534	0.358	0.062	0.598

TABLE 3.4: School average performance of 23-fish wide school.

Finally, the effect of making the school wider is examined by adding additional dense diamond sub-units in the spanwise direction, resulting in a 23-fish wide school. The school-averaged results are shown in Table 3.4. Compared to the 10-fish school, there is an increase in both average thrust production and power consumption, resulting in a slight increase in the net efficiency, however, C_x is significantly reduced, indicating that the drag on the school has increased. This makes intuitive sense, as the frontal area of the school has increased from $0.4l$ to $0.8l$. The vorticity and cycle-averaged streamwise velocity are shown in Fig. 3.17. The wake behind the school has flipped to a BvK center, indicating a drag wake, with two pairs of 2P vortex streets neighboring the center street. The inner vortex from the 2P pairs propagates downstream alongside
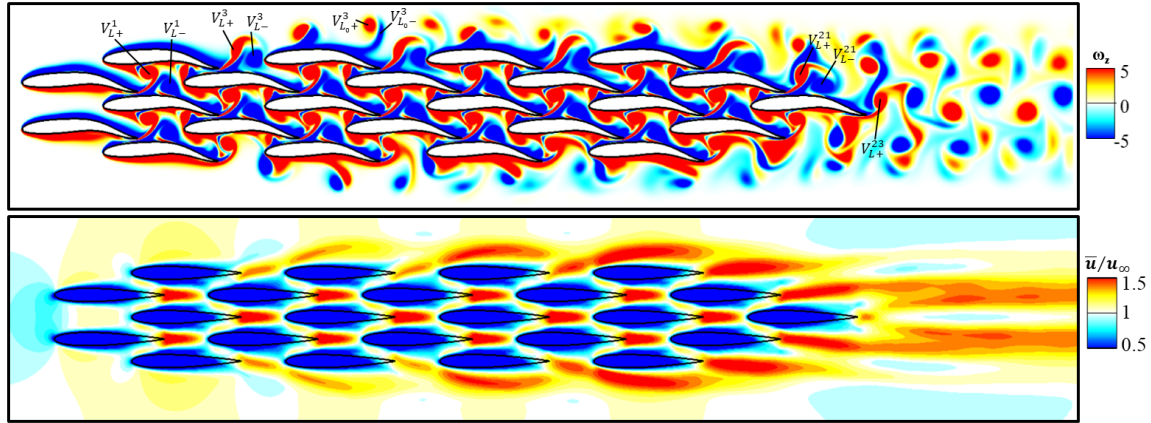
FIGURE 3.17: Vorticity at $t/T = 0.18$ (a) and cycle averaged streamwise velocity (b) in the 23-fish wide school.

the middle street, creating jets due to the proximity of the opposite sign vortices from each source, resulting in two weaker jets behind the school, occurring between the 2s and 2P wake components. The weaker jets, along with a larger school, indicate that less momentum is propagated downstream to result in thrust for the fish school. This is reflected in the reduced C_x average compared to the narrower 10 and 16 fish schools. Within the school, near-body vortices remain similar to those observed for the 10-fish school. In the front, middle, and back fish, the same vortex pair trapped inside the channel is observed in V_{L+}^1 and V_{L-}^1. Because they are fully contained by the channel, there is little opportunity for any change in the behavior of the vortex pair. In the back fish, the same single vortex V_{L+}^{23} is generated, however, it has destructive interaction with the preceding back-edge fish vortex pair V_{L-}^{21}, where there was previously no interaction between the two. Finally, the edge fish has a similar vortex pair V_{L+}^3 and V_{L-}^3 that is shed from one edge fish and partially interacts with subsequent edge fish.

Finally, the longer school is grouped similarly, and the results are shown in Fig. 3.18.
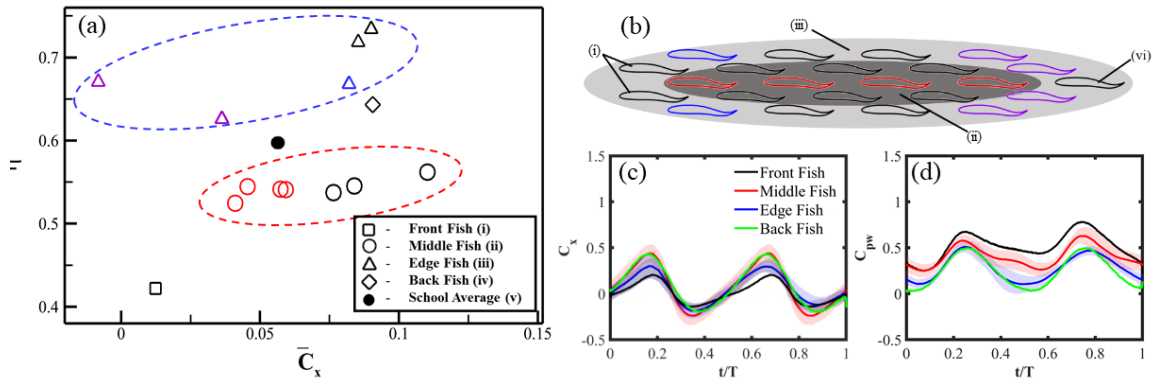
FIGURE 3.18: Vorticity at the peak thrust production (t = 9.18T) for $Re = 2000$ (a) and $Re = 4000$ (b).

The same zones of high efficiency and high net force from the edge and middle, respectively, are observed in part (a). A new sub-group within the middle fish is identified as the center-middle fish, indicated in red, with a lower C_x than the other middle fish, as there is even less opportunity for lateral advection of momentum besides the fish as there are multiple fish bodies between them and the edge of the school. As shown from the wall effect, this lowers the peak thrust produced during the tail flapping.

3.3 Conclusion

The performance of the fish within the school is found to be significantly improved by swimming within a school rather than alone, and the benefit is further increased in the large school compared to previous studies of smaller schools. The vortex interactions and wake is analyzed, and the enhanced performance of individual fish within the school is shown to be caused by incoming vortex interactions, block effect, wall effect, and anterior body suction effect. These mechanisms are entirely dependent on the arrangement of the surrounding fish, so intuitive classifications of individual fish

are formed based on the position of neighboring fish. They categorize fish into front fish, edge fish, middle fish, and back fish, with further subcategories of the edge fish of front-edge fish and back-edge fish. Hydrodynamic performance of individual fish in large schools shows similar performance between individuals within each group, strengthening the physical basis for the classifications chosen and leading to the major performance zones of the high-efficiency edge fish and the high net force middle fish are predicted, along with the low-efficiency front fish and high efficiency back fish. These mechanisms and groupings are robust to changes in Reynolds number, length of the school, and width of the school.

4 Effect of Increasing School Length

4.1 Arrangements

In studies of in-line flapping foils, a limit is approached around 5 foils for hydrodynamic performance improvement from adding foils [16]. A similar result is expected in fish schools, as it is impossible for the performance increase from the 4-fish dense diamond school to the 10-fish school in Chapter 3 to continue infinitely. Real fish schools, however, can have millions of fish and are of significant length. To investigate this effect, the dense diamond school is used as a baseline, and the length of the school is increased by adding subsequent diamonds onto the back of the school. This is detailed in Fig. 4.1. In the figure, additional units are shown in blue and red, and more are added for this study, up to 25. The spacing is given by D, m, and e, which are all set to $0.4l$ to be in line with the dense diamond school defined in Pan and Dong [20], [21].
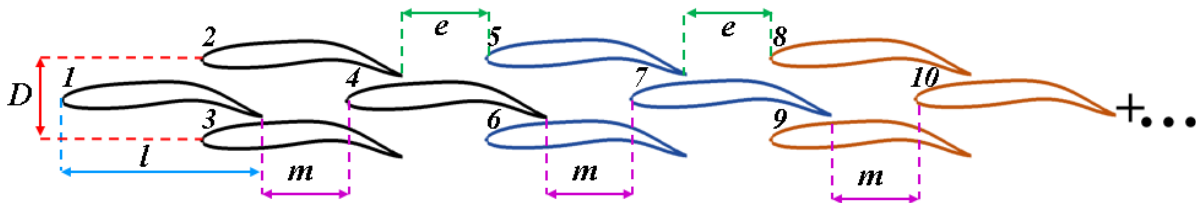

FIGURE 4.1: Increasing length of the school based on dense diamond baseline.

4.2 Results

4.2.1 School Average Performance

To study the effect of length on the performance, the baseline configuration shown in Fig. 4.1 is run for $N_{school} = 4$ to $N_{school} = 25$. The results are shown in FIG. 4.2. In the figure the red line shows the school averaged efficiency, (η_*). The asterisk (*) denotes the school averaged value. The blue line shows the school averaged cycle averaged force coefficient in the x direction, (C_x^*). The overline ($\bar{}$) denotes the cycle averaged value. N_{school} denotes the number of fish in the school. First, the thrust (a) and power (c) both have the same overall trend, with a steady increase in both thrust produced and power consumed as the school increases in length. In power consumption, the middle fish increase more than the others.

In the efficiency (d), a steep increase in the average is seen from 4 to 10 fish, increasing by 7 from $N_{school} = 4$ to $N_{school} = 10$. The efficiency improvement then slowly flattens out, with just 3.5% increase in efficiency from $N_{school} = 10$ to $N_{school} = 25$. This sug-gests that for schools larger than 25 fish, the improvement in efficiency will continue to flatten out until it is essentially zero. Also, a slight drop in efficiency is observed from $N_{school} = 10$ to $N_{school} = 13$, breaking the overall trend of efficiency increasing as the number of fish in the school increases. The increase in efficiency comes largely from the edge fish, while the middle has little change in efficiency as the length of the school increases.

The average force coefficient in the x direction behaves similarly, increasing sharply

from $N_{school} = 4$ to $N_{school} = 10$. It then flattens out, with a very small increase from $N_{school} = 10$ to $N_{school} = 13$. It then drops constantly from $N_{school} = 10$ to $N_{school} = 25$. This peak shows that the best performing long schools have 10 or 13 fish in them, while increasing the school past 25 fish will lead to continued decrease in (C_x^*). The middle fish increase throughout, but start to approach a limit at $N_{school} = 25$. The edge fish follow the same trend as the averages, increasing to a peak at $N_{school} = 10$ and steadily dropping as more fish are added.

To understand these results further, $\overline{C_x}$ is plotted with η for every fish in the school in Fig. 4.3. In the figure, the color denotes the length of the school for the fish, with a contour from red for the shortest school to blue for the longest school. The fish shapes utilize the groupings defined in Chapter 3. Once again, the groupings correlate closely with distinct performance zones, confirming the groupings are sensible for the dense long schools. The front fish are the lowest efficiency, but increase in both η and $\overline{C_x}$ as the length of the school increase. A similar trend is seen in the middle fish, where most of the highest η and $\overline{C_x}$ middle fish are in longer schools. The edge fish however have a large drop in $\overline{C_x}$ in some of the longer schools, with some of the fish producing less net force than a single fish swimming. This confirms that the drop-off observed in Fig. 4.2 occur due to the edge fish in the school.
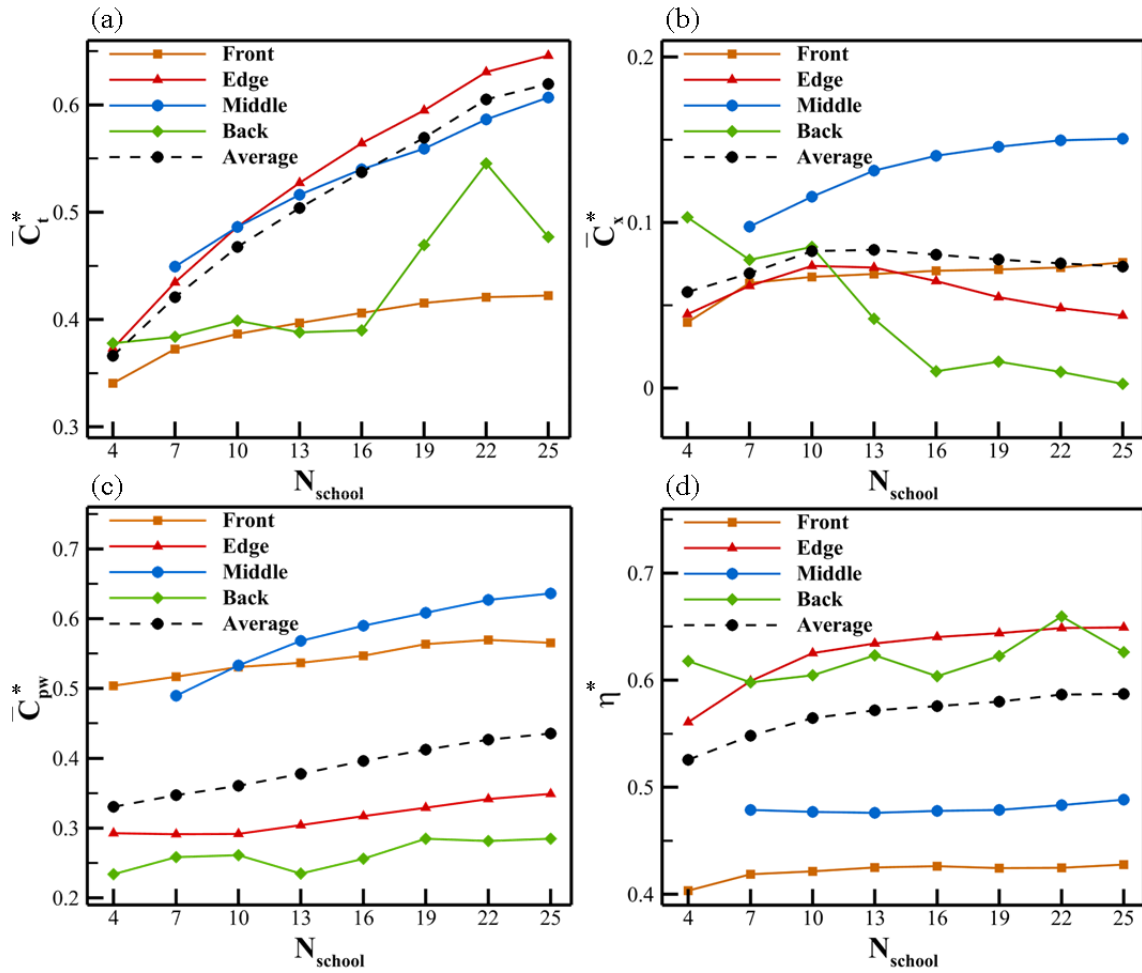
FIGURE 4.2: $\overline{C_t}^*$ (a), $\overline{C_x}^*$ (b), $\overline{C_p}^*$ (c), and $\overline{\eta}^*$ (d) varying with change in length of the fish school.
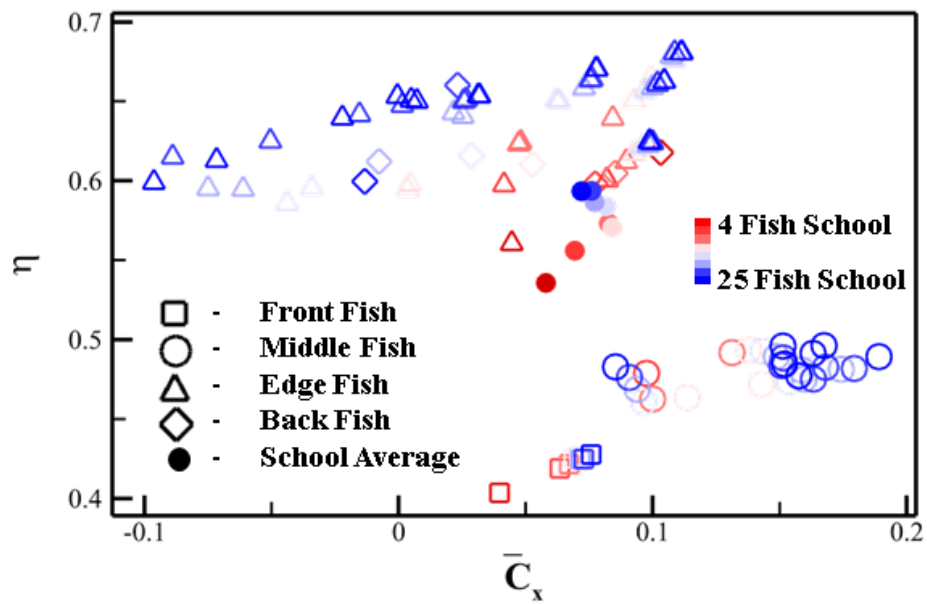
FIGURE 4.3: Net force vs Efficiency for every fish in the long schools. The color indicates the length of the school and the shape indicates the group of the fish.

4.2.2 Subgroups Within Long Schools

Next, the fish are combined into subgroups in a similar method to how they are cre-

ated in Fig 4.1. The front fish, along with the back three fish, are excluded from the

grouping, as these fish are on the outside of the school and have significantly different

performance from the patterns of the more central fish. This definition is shown in

4.4(a), with G_i denoting the subgroup number, each made up of three fish. For each

school size, there are $(N_{school} - 4)/3$ subgroups. The cycle averaged force in the x di-

rection is averaged over the three fish in each group and plotted in Fig. 4.4(b). This

plot shows the trend for each school size, with $N_{school} = 4$ shown in red and $N_{school} = 25$

shown in blue. The overall trend across all the school sizes is immediately clear. The

$\overline{C_x}$ values increase from the front of the school to $G = 3$, then drop off steeply until

the end of the school. This explains well the overall trend seen in Fig. 4.2(b), where

the values increase up to $N_{school} = 13$ and then drops off. $N_{school} = 13$ corresponds to

$G = 3$, so each additional group added to the school lowers the school average val-

ues. Additionally, a sharp drop in $\overline{C_x}$ from the general downward trend is observed

in the last group for all schools with $G = 4$ or larger. In the data for the last 3 fish, ex-

cluded by the grouping definition, a similar drop off occurs for all schools larger than

$N_{school} = 10$, explaining why the values for $N_{school} = 10$ and $N_{school} = 13$ are very close.

Additionally, there is a general trend of higher $\overline{C_x}$ values as the school gets larger is ob-

served. The improvement decreases with each additional group added to the school,

and is approximately zero from $N_{school} = 19$ to $N_{school} = 22$. This shows that the drop

in performance is not unique to a certain length of school, and occurs at the same point
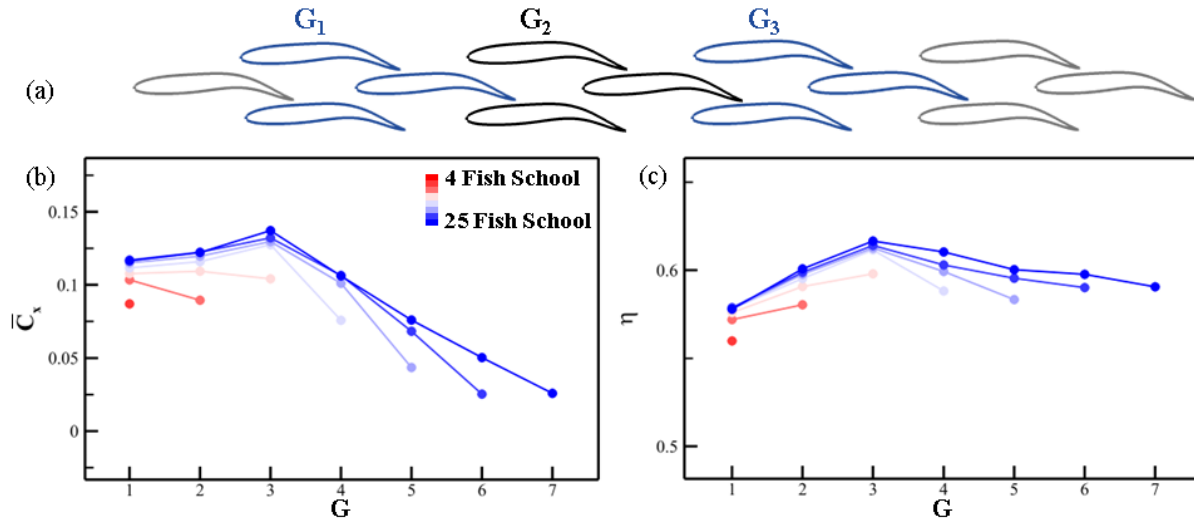
FIGURE 4.4: Performance average of each added subgroup. Part (a) demonstrates the definition for subgroups on a 13 fish school. Parts (b) and (c) show the average $\overline{C_x}$ and $\overline{\eta}$ values respectively.

along the school for all longer schools in the study.

The efficiencies are similarly plotted for each three fish group average for every school size, shown in Fig 4.4(c). The plot shows the group averaged efficiency for every group within each school size, with $N_{school} = 4$ shown in red and $N_{school} = 25$ shown in blue. A similar trend is shown to $\overline{C_x}$, with efficiencies reaching a maximum at $G = 3$ and decreasing along the school after that point. In the data for the last 3 fish, a drop in efficiency is observed for all except the 10 fish school, which sees a similar increase to the schools shown from $G = 2$ to $G = 3$. This is strong evidence that there is a hydrodynamic phenomenon occurring at the addition of the 3rd group, giving peak η and $(C_x^)$ values for these fish. In addition, Fig 4.4(c) shows a slight increase in the overall values as the school gets larger. This improvement decreases with each additional group added to the school, similar to the trend in $(C_x^)$, and is approximately zero from $N_{school} = 13$ to $N_{school} = 16$. Finally, from the larger schools in this plot, we see that

adding further fish continues to see a drop in efficiency from the peak at $G = 3$, how-ever it is still higher than the lowest values at $G = 1$. From this, we can expect the school average values shown Fig 4.2(d) to continue to flatten as the school size goes past 25 fish.

4.2.3 Flow Analysis in Long Schools

To begin an analysis of the flow in longer schools, the vorticity for the 7, 13, 19, and 25 fish schools are shown in Fig. 4.5. Overall, the vortex structures for each group represented in Fig. 3.4 are still present in the near body vortices. The most apparent change in the near body wakes as the school lengthens is the collapse of the vortex pair behind each edge fish, which stays closer to the center of the school as the length of the school increases. This can easily be seen at the back of the school, where the back edge fish on top has an increasingly less lateral advection of the vortex pair. This occurs due to the increasing number of fish in front contributing to streamwise flow that keeps the vortex from stretching laterally. Evidence for this can be seen in Fig. 4.6, which shows the cycle averaged streamwise velocity for the same schools. In the figure, the edge jets increase in length and strength as fish are added to the school. The stronger jets prevent lateral advection and lead to the overall narrowing effect seen in Fig. 4.5. In the wake, the center 2S pair, along with 2P pairs on either side, continues to be the overall structure for all lengths. Despite the overall structure being present, however, the consistency and prevalence of the 2P wake parts decreases as the school length increases, until the 2P is a minor part of the wake that dissipates quickly in the
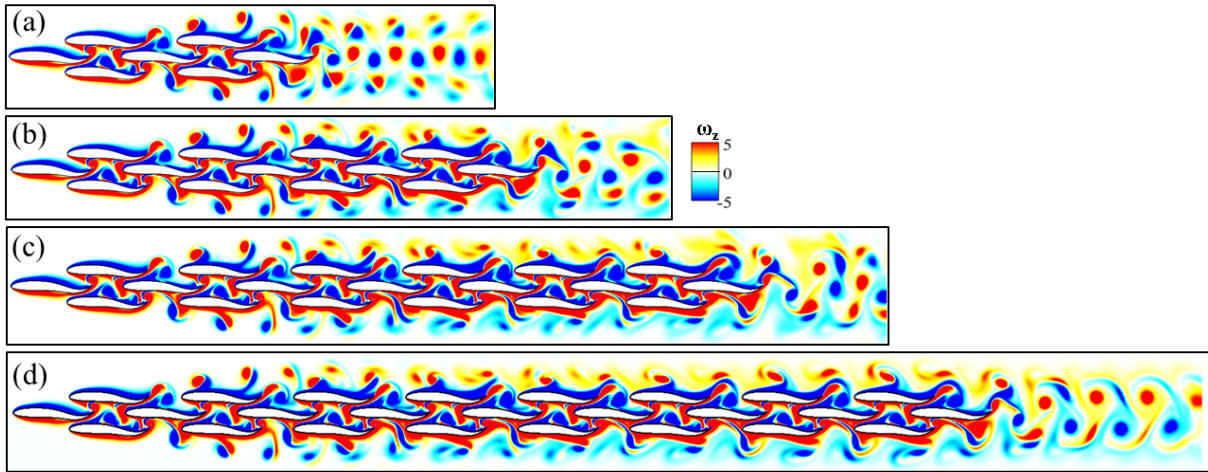
FIGURE 4.5: Vorticity at $t/T = 1.0$ for $N_{School} = 7, 13, 19, 25$.
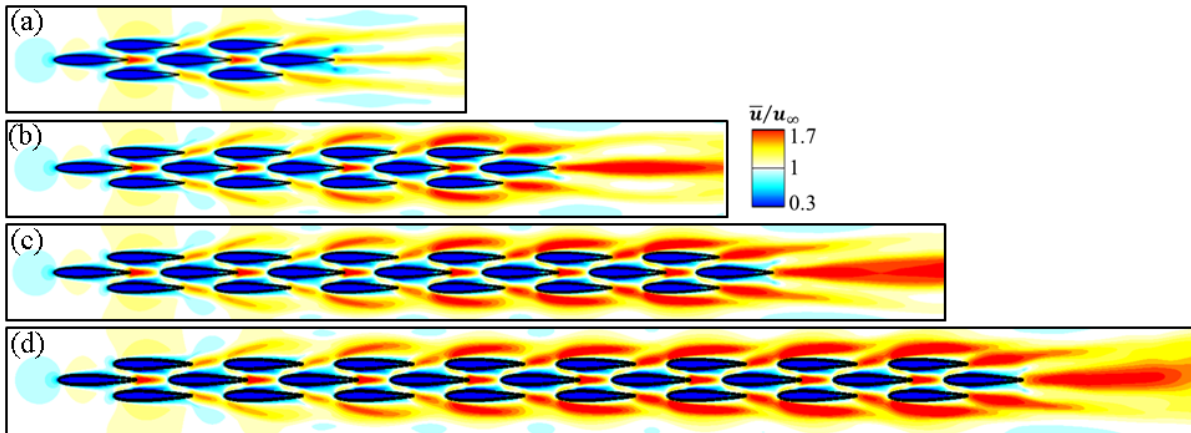
FIGURE 4.6: Cycle average streamwise velocity for $N_{School} = 7, 13, 19, 25$.

$N_{school} = 25$ wake. The 2S core, on the other hand, maintains a consistent presence throughout the schools. The rBvK structure is seen in all schools $N_{school} \geq 7$, and the lateral spacing between increases as the length of the school increases. This is overall beneficial as shown in Pan and Dong [21], however in the previous results a wider spacing between vortices is not necessarily beneficial, and many of the top results in C_x were shown to have a narrower wake. This is also observed in the current study, where the widening of the 2S wake structure corresponds with a drop in C_x for the school. Similar results are seen in Fig. 4.6, where the center jet increases in magnitude and width as the school gets longer. This is expected, as more fish bodies in the flow should correspond to more momentum flowing downstream. The short jets on the edge fish increase in size and strength as the length of the school increases.

4.2.4 Body-Body Interaction Mechanisms in Long Schools

Next, the fish-fish interaction mechanisms detailed in Chapter 3 are discussed as the length of the school increases. First, the wall effect is investigated using the same instantaneous velocity at $t/T = 1.0$, plotted for $N_{School} = 20$ in Fig. 4.7. In the figure, the middle fish have a very consistent instantaneous jet throughout the school. The edge fish also have a similar pattern, however the size of the jet increases, indicating an increase in the downstream momentum redirection due to the wall effect for the
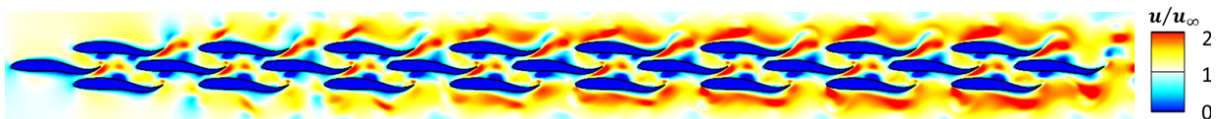

FIGURE 4.7: Instantaneous streamwise velocity at $t/T = 1.0$ for $N_{School} = 25$.
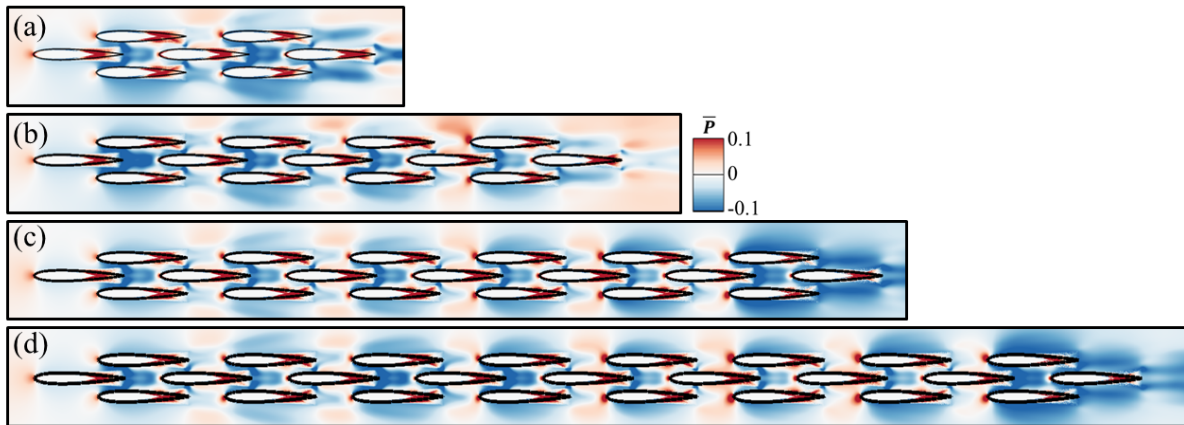
FIGURE 4.8: Cycle averaged pressure for $N_{School} = 7, 13, 19, 25$.

edge fish. This suggests a slight increase in the wall effect portion of C_x values as the school length increases.

The block effect is discussed utilizing the cycle averaged pressure for the 7, 13, 19, and 25 fish schools, shown in Fig 4.8. In the figure, a similar low pressure region behind each fish is shown, and there is no significant change in the magnitude along the school observed. In numerically comparing the average pressure behind each fish, it is seen that the length changes in the school lead to no consistent change in pressure between fish, and that the enhanced block effect due to more than 1 fish behind in a line is limited to 2 additional fish. This means the enhanced block effect occurs throughout the school, but the drop in performance from lack of enhanced block effect only occurs in the second to last fish in a given line.

Finally, the effect of increasing length on anterior body suction is investigated first by averaging C_x on the anterior (front 30%) of each fish over the cycle. These results are then averaged amongst the edge fish, middle fish, and whole school, and are plotted in
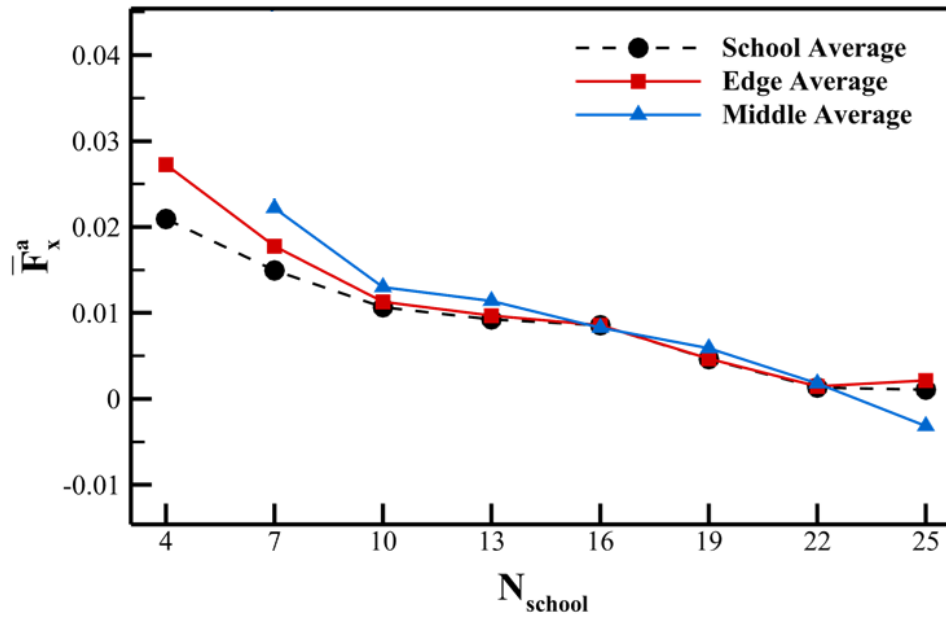
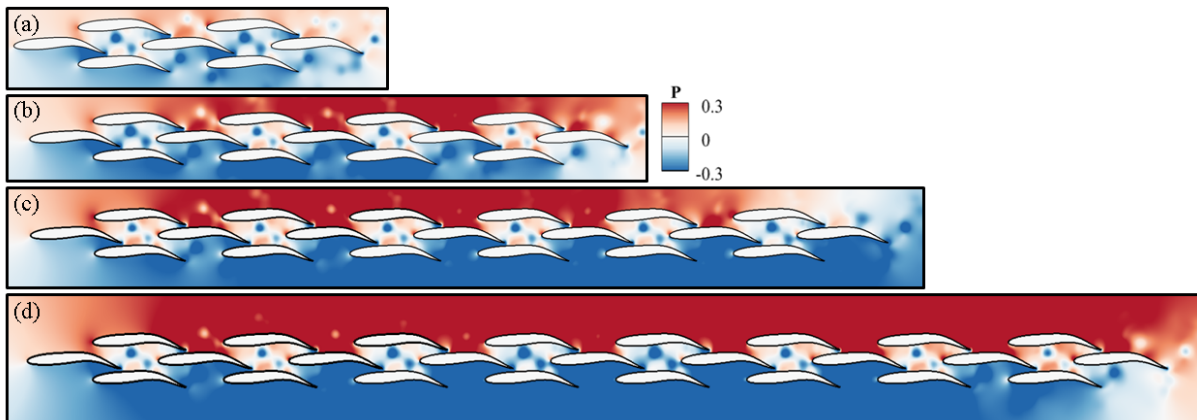FIGURE 4.9: Cycle averaged C_x^a in schools of increasing length.

FIGURE 4.10: Instantaneous pressure at $t/T = 0.25$ for $N_{School} = 7, 13, 19, 25$.

Fig. 4.9. In the figure, a consistent drop in the school, edge, and middle average ante-

rior body suction result from increasing the length of the school. To explain this result,

the instantaneous pressure for the 7, 13, 19, and 25 fish schools are shown in Fig. 4.10.

In the figure, the pressure on the outside of the school, which was shown in Chapter

3 to follow the same trend as a single fish swimming, increasing in magnitude signif-

icantly as fish are added. This makes sense, as the fish are swimming synchronously

so the low and high pressure regions are similar for all fish at once. As the bottom of

the fish becomes low pressure and the top becomes high pressure for the entire school,

larger low and high pressure regions form, as seen in the figure. Because of this, the

anterior body for individual fish are more influenced by this overall shape rather than

nearest neighboring fish. For example, in the figure the top edge fish create a low pres-

sure zone that creates suction on the top half of the middle fish in the 7 fish school

(a). In the longest school, however, the top edge fish do not overcome the trend of the

whole school and the entire top half remains high pressure, preventing any suction

from occurring (d). This causes net pressure effects on the head of the fish to cancel

out, resulting in a trend towards $\overline{F_x^a} = 0$ which is seen in Fig. 4.9.

4.3 Conclusion

The efficiency of the school is found to increase with increasing the length of the school,

however a limit is reached near $N_{School} = 19$. A maximum $\overline{C_x}$ value is found around

$N_{School} = 13$, after which the performance of the school drops off. This if found to occur

due to a breakdown in the vortex structure along the edges of the school, caused by the

wake from previous fish along the edge interacting with subsequent edge fish wakes. The wall effect is shown to behave similarly within longer schools. The block effect is also consistent, and the enhanced block effect is limited to 2 fish bodies blocking the flow behind a fish to further enhance its performance.

5 Conclusions

5.1 Summary of Accomplishments

Utilizing high-fidelity numerical simulations, the hydrodynamics of 2D dense synchronous large fish schools are studied in depth. In Chapter 3, the interactions within a large fish school are observed, and the vortex structures and wake are characterized. From this, the wall effect, block effect, and anterior body suction, along with interactions with oncoming vortices are established as primary interactions within large dense schools. Understanding of these mechanisms is increased as they are applied to large schools, and the enhanced and partial block effect are discussed. The wall effect and anterior body suction are shown to occur throughout the school, as in previous discussions they were mentioned only in the context of a single fish on the edge and back of a diamond, respectively. From these effects, it is shown that primary interactions and performance are dependent on the arrangement of neighboring fish, and thus individual fish can be categorized based on their spatial arrangements. From this, the front, middle, edge, and back fish groups are shown to be distinct in their interactions and performance within the large school. These groupings are proven to be independent of arrangement and Reynolds number, and the changes in vortex structures and wake

for these parameters are discussed. In Chapter 4, the effects of increasing the length of the school by adding additional fish are observed. The efficiency approaches a limit, whereas the net force for the school reaches a maximum followed by a decline as the length of the school increases. This is shown to occur primarily due to breakdown in the vortex structures along the edge of the school and the anterior body suction as the length increases.

The significance of this work is three-fold. First, it offers an initial look into the hydro-dynamics of large fish schools using a high-fidelity model, improving on the previous works using a small number of fish or low-order models. In this investigation, the rules for hydrodynamic interaction are tested and applied in the setting of a large school, and previously defined effects are shown implemented in larger schools. Second, from the performance and hydrodynamics of the school, categorizations are elucidated that group the fish with similar performance and interactions. These groupings are proved to be robust and serve as a method for understanding larger schools in the future. Fi-nally, the effects of increasing length in a school give an initial insight as to the limits of possible benefits from increasing the number of individuals in a school. In addition to direct impacts in understanding fish schools observed in biology, this work also serves to inform bio-inspired underwater vehicle design, as well as broader applications of high-efficiency unsteady flow applications with a large number of bodies.

5.2 Future Work

The results from our work show high-efficiency large fish schools can be formed using the dense diamond as a baseline. School-averaged performance shows that valuable gains can be made from using large numbers of fish in a school, however many assumptions had to be made to enable the study. In future work, these assumptions can be tested to see how wide the application of the mechanisms discussed is. In particular, the effects of 3D, synchrony, and school density can be tested. Additionally, the stability of the school is not considered, as this thesis focused on the hydrodynamics and interactions between fish. To enable large dense schools in future robotics platforms, additional work is required on finding stable configurations, either via hydrodynamic interactions or active control.

Bibliography

[1] D. Weihs, "Hydromechanics of fish schooling," *Nature*, vol. 241, pp. 290–291, 1973.

[2] C. H. White, G. V. Lauder, and H. Bart-Smith, "Tunabot Flex: A tuna-inspired robot with body flexibility improves high-performance swimming," *Bioinspiration and Biomimetics*, vol. 16, no. 2, 2021.

[3] G. J. Dong and X. Y. Lu, "Characteristics of flow over traveling wavy foils in a side-by-side arrangement," *Physics of Fluids*, vol. 19, no. 5, 2007.

[4] M. S. U. Khalid, I. Akhtar, and H. Dong, "Hydrodynamics of a tandem fish school with asynchronous undulation of individuals," *Journal of Fluids and Structures*, vol. 66, pp. 19–35, 2016.

[5] X. Lin, J. Wu, L. Yang, and H. Dong, "Two-dimensional hydrodynamic schooling of two flapping swimmers initially in tandem formation," *Journal of Fluid Mechanics*, vol. 941, no. A29, pp. 1–17, 2022.

[6] G. Novati, S. Verma, D. Alexeev, D. Rossinelli, W. M. Van Rees, and P. Koumoutsakos, "Synchronisation through learning for two self-propelled swimmers," *Bioinspiration and Biomimetics*, vol. 12, no. 3, 2017.

[7] S. Verma, G. Novati, and P. Koumoutsakos, "Efficient collective swimming by harnessing vortices through deep reinforcement learning," *Proceedings of the National Academy of Sciences of the United States of America*, vol. 115, no. 23, pp. 5849–5854, 2018.

[8] G. Li, D. Kolomenskiy, H. Liu, B. Thiria, and R. Godoy-Diana, "On the energetics and stability of a minimal fish school," *PLoS ONE*, vol. 14, no. 8, pp. 1–20, 2019.

[9] Y. Pan, W. Zhang, and H. Dong, "Computational Modeling and Hydrodynamic Analysis of Fish Schools in Three-Dimensional Arrangements," *FEDSM2022*, 2022.

[10] M. P. O'Neill, "Mullet mania," *Hakai Magazine*, 2018.

[11] D. Pavlov and A. Kasumyan, "Patterns and mechanisms of schooling behavior in fish: A review," *Journal of Ichthyology*, vol. 40, no. 2, pp. 163–231, 2000.

[12] M. Gazzola, A. A. Tchieu, D. Alexeev, A. De Brauer, and P. Koumoutsakos, "Learning to school in the presence of hydrodynamic interactions," *Journal of Fluid Mechanics*, vol. 789, pp. 726–749, 2016.

[13] A. Filella, F. Nadal, C. Sire, E. Kanso, and C. Eloy, "Model of Collective Fish Behavior with Hydrodynamic Interactions," *Physical Review Letters*, vol. 120, no. 19, 2018.

[14] A. Kaganovsky, "The school composition and the behavior of far east sardine with respect to oceanographic conditions," *Doct. Sci. (Biol.) Dissertation*, 1942.

[15] D. Radakov and A. Mochek, "On the mutual stimulation in schools of pritella riddlei meek and rhodeus sericeus (pallas)," *Copr. Ikhtiol*, vol. 12, no. 3, pp. 582–584, 1972.

[16] C. Yuan, G. Liu, Y. Ren, and H. Dong, "Propulsive performance and vortex interactions of multiple tandem foils pitching in line," *45th AIAA Fluid Dynamics Conference*, no. June, pp. 1–11, 2015.

[17] P. Han, Y. Pan, G. Liu, and H. Dong, "Propulsive performance and vortex wakes of multiple tandem foils pitching in-line," *Journal of Fluids and Structures*, vol. 108, p. 103 422, 2022.

[18] M. Saadat, F. Berlinger, A. Sheshmani, R. Nagpal, G. V. Lauder, and H. Haj-Hariri, "Hydrodynamic advantages of in-line schooling," *Bioinspiration and Biomimetics*, vol. 16, no. 4, 2021.

[19] L. Dai, G. He, X. Zhang, and X. Zhang, "Stable formations of self-propelled fish-like swimmers induced by hydrodynamic interactions," *Journal of the Royal Society Interface*, vol. 15, no. 147, 2018.

[20] Y. Pan and H. Dong, "Computational analysis of hydrodynamic interactions in a high-density fish school," *Physics of Fluids*, vol. 32, no. 12, 2020.

[21] Y. Pan and H. Dong, "Effects of phase difference on hydrodynamic interactions and wake patterns in high-density fish schools," *Physics of Fluids*, vol. 34, no. 111902, pp. 1–25, 2022.

[22] A. Menzer, Y. Gong, F. E. Fish, and H. Dong, "Bio-Inspired Propulsion : Towards Understanding the Role of Pectoral Fin Kinematics in Manta-like Swimming," *Biomimetics*, vol. 7, no. 45, 2022.

[23] G. Liu, Y. Ren, H. Dong, O. Akanyeti, J. C. Liao, and G. V. Lauder, "Computational analysis of vortex dynamics and performance enhancement due to body-fin and fin-fin interactions in fish-like locomotion," *Journal of Fluid Mechanics*, vol. 829, pp. 65–88, 2017.

[24] J. Wang, D. K. Wainwright, R. E. Lindengren, G. V. Lauder, and H. Dong, "Tuna locomotion: A computational hydrodynamic analysis of finlet function," *Journal of the Royal Society Interface*, vol. 17, no. 165, 2020.

[25] P. Han, G. Liu, Y. Ren, and H. Dong, "Computational Analysis of 3D Fin-Fin Interaction In Fish's Steady Swimming," *FEDSM2016*, pp. 1–6, 2016.

[26] J. Kelly, H. Pan, H. Dong, and T. Van Buren, "Wake Structures and Effect of Hydrofoil Shapes in Efficient Flapping Propulsion," *FEDSM2021*, pp. 1–7, 2021.

[27] J. Kelly, Y. Pan, and H. Dong, "Body Shape Effects on the Hydrodynamic Performance of Bio-Inspired Undulating Swimmers," *FEDSM2022*, pp. 1–6, 2022.

[28] M. S. U. Khalid, J. Wang, H. Dong, and M. Liu, "Flow transitions and mapping for undulating swimmers," *Physical Review Fluids*, vol. 5, no. 6, p. 63 104, 2020.

[29] C. Li, H. Dong, and G. Liu, "Effects of a dynamic trailing-edge flap on the aerodynamic performance and flow structures in hovering flight," *Journal of Fluids and Structures*, vol. 58, pp. 49–65, 2015.

[30] M. Bozkurttas, H. Dong, V. Seshadri, R. Mittal, and F. Najjar, "Towards numerical simulation of flapping foils on fixed cartesian grids," *43rd AIAA Aerospace Sciences Meeting and Exhibit - Meeting Papers*, no. December 2014, pp. 15 801–15 809, 2005.

[31]   R. Mittal, H. Dong, M. Bozkurttas, F. M. Najjar, A. Vargas, and A. von Loebbecke, "A versatile sharp interface immersed boundary method for incompressible flows with complex boundaries," *Journal of Computational Physics*, vol. 227, no. 10, pp. 4825–4852, 2008.

[32]   P. A. Dewey, D. B. Quinn, B. M. Boschitsch, and A. J. Smits, "Propulsive performance of unsteady tandem hydrofoils in a side-by-side configuration," *Physics of Fluids*, vol. 26, no. 4, 2014.

[33]   J. J. VIDELER and F. HESS, "Fast Continuous Swimming of Two Pelagic Predators, Saithe (Pollachius Virens) and Mackerel (Scomber Scombrus): a Kinematic Analysis," *Journal of Experimental Biology*, vol. 109, no. 1, pp. 209–228, 1984.

[34]   Y. Pan, P. Han, J. Huang, and H. Dong, "Effect of Formation Pattern on Schooling Energetics in Fish-Like Swimming," *FEDSM2020*, pp. 1–8, 2020.

[35]   C. K. Hemelrijk, D. A. Reid, H. Hildenbrandt, and J. T. Padding, "The increased efficiency of fish swimming in a school," *Fish and Fisheries*, vol. 16, no. 3, pp. 511–521, 2015.

[36]   S. S. Killen, S. Marras, J. F. Steffensen, and D. J. Mckenzie, "Aerobic capacity influences the spatial position of individuals within fish schools," *Proceedings of the Royal Society B: Biological Sciences*, vol. 279, no. 1727, pp. 357–364, 2012.

[37]   S. Marras and P. Domenici, "Schooling Fish Under Attack Are Not All Equal: Some Lead, Others Follow," *PLoS ONE*, vol. 8, no. 6, 2013.

[38]   M. Daghooghi and I. Borazjani, "The hydrodynamic advantages of synchronized swimming in a rectangular pattern," *Bioinspiration and Biomimetics*, vol. 10, no. 5, 2015.

[39] D. B. Quinn, K. W. Moored, P. A. Dewey, and A. J. Smits, "Unsteady propulsion near a solid boundary," *Journal of Fluid Mechanics*, vol. 742, pp. 152–170, 2014.

[40] D. B. Quinn, G. V. Lauder, and A. J. Smits, "Flexible propulsors in ground effect," *Bioinspiration and Biomimetics*, vol. 9, no. 3, 2014.